

A fourth-order accurate finite volume scheme for resistive relativistic MHD

A. Mignone¹,^{*} V. Berta¹, M. Rossazza¹, M. Bugli^{1,2,3}, G. Mattia⁴, L. Del Zanna^{5,4,6}, and L. Pareschi^{7,8}

¹*Dipartimento di Fisica, Università degli Studi di Torino, Via Pietro Giuria 1, I-10125 Torino, Italy*

²*INFN - sezione di Torino, Via Pietro Giuria 1, I-10125 Torino, Italy*

³*Université Paris-Saclay, Université Paris Cité, CEA, CNRS, AIM, F-91191, Gif-sur-Yvette, France*

⁴*INFN - sezione di Firenze, Via G. Sansone 1, I-50019 Sesto Fiorentino (FI), Italy*

⁵*Dipartimento di Fisica e Astronomia, Università degli Studi di Firenze, Via G. Sansone 1, I-50019 Sesto Fiorentino (FI), Italy*

⁶*INAF - Osservatorio Astrofisico di Arcetri, L.go E. Fermi 5, I-50125 Firenze, Italy*

⁷*Maxwell Institute for Mathematical Sciences and Department of Mathematics, Heriot-Watt University, Colin Maclaurin Building, Edinburgh, EH14 4AS, United Kingdom*

⁸*Dipartimento di Matematica e Informatica, Università degli Studi di Ferrara, Via N. Machiavelli 30, I-44121 Ferrara, Italy*

Accepted XXX. Received YYY; in original form ZZZ

ABSTRACT

We present a finite-volume, genuinely 4th-order accurate numerical method for solving the equations of resistive relativistic magnetohydrodynamics (Res-RMHD) in Cartesian coordinates. In our formulation, the magnetic field is evolved in time in terms of face-average values via the constrained-transport method while the remaining variables (density, momentum, energy and electric fields) are advanced as cell volume-averages. Spatial accuracy employs 5th-order accurate WENO-Z reconstruction from point values (as described in a companion paper) to obtain left and right states at zone interfaces. Explicit flux evaluation is carried out by solving a Riemann problem at cell interfaces, using the Maxwell-Harten-Lax-van Leer with contact wave resolution (MHLLC). Time stepping is based on the implicit-explicit (IMEX) Runge-Kutta (RK) methods, of which we consider both the 3rd-order strong stability preserving SSP3(4,3,3) and a recent 4th-order additive RK scheme, to cope with the stiffness introduced by the source term in Ampere’s law. Numerical benchmarks are presented in order to assess the accuracy and robustness of our implementation.

Key words: magnetic reconnection - methods: numerical - (magnetohydrodynamics) MHD - plasma - relativistic processes – software: development

1 INTRODUCTION

The investigation of relativistic plasma dynamics holds crucial importance in understanding the complex nature of high-energy astrophysical phenomena. Under typical astrophysical conditions, resistivity remains exceptionally low, and the ideal framework well describes processes occurring on rapid time scales. Nevertheless, the evolving flow dynamics can cause the formation of local regions with steep gradients, such as current sheets, where the influence of resistivity can no longer be ignored.

It appears then clear the necessity of numerical simulations of astrophysical plasmas beyond the ideal magnetohydrodynamics (MHD) assumptions. Resistive Relativistic Magnetohydrodynamics (Res-RMHD) is indeed a framework that takes into account the contribution of finite plasma conductivity. In Res-RMHD, the comoving electric field no longer vanishes as in ideal MHD and it is directly proportional to the local current density, which is characterized by a scalar resistivity coefficient denoted as η .

Numerical methods for the solutions of the Res-RMHD equations have been now presented by a number of authors in the context of 2nd-order conservative schemes (see, for instance, Palenzuela et al. 2009; Komissarov 2007; Bucciantini & Del Zanna 2013; Dionysopoulou et al. 2013; Mizuno 2013; Miranda-Aranguren et al. 2018; Mignone

et al. 2019; Cheong et al. 2022; Nakamura et al. 2023, and references therein) or higher order schemes (Dumbser & Zanotti 2009; Del Zanna et al. 2014; Bugli et al. 2014; Tomei et al. 2020).

A delicate aspect for their robust implementation is the stability of the method while dealing with the stiff relaxation term in Ampere’s law, posing very strict constraints for time-explicit calculations. This makes the implementation of Res-RMHD numerical schemes more challenging than their ideal counterpart. In this sense, the employment of implicit–explicit Runge–Kutta (IMEX, see Pareschi & Russo 2005) represents an effective solution to the problem, allowing larger time steps to overcome stiffness.

Another important aspect is related to the divergence-free condition and charge conservation which are not automatically fulfilled at the discrete level. To cope with this issue, here we follow an approach similar to Mignone et al. (2019) (paper I henceforth), by adopting the constrained transport (CT) approach to control the divergence of magnetic field. In the CT formalism (see Evans & Hawley 1988; Balsara & Spicer 1999; Londrillo & del Zanna 2004; Mignone & Del Zanna 2021, and references therein) the magnetic field components are evolved as area-weighted quantities positioned on the faces orthogonal to the corresponding component direction. This ensures that the condition $\nabla \cdot \nabla \times \mathbf{E} = 0$ is satisfied also at discrete level. In paper I, the CT method has been extended to control the divergence of the electric field as well, thus ensuring a consistent approach for charge conservation. The resulting scheme has shown to be more

* E-mail: andrea.mignone@unito.it

robust when compared to cell-centered frameworks such as the generalized Lagrange multipliers (GLM, [Munz et al. 2000](#); [Dedner et al. 2002](#)). In the present work, however, we choose to constrain only the magnetic field and evolve the electric field as a zone-centered variable without explicitly enforcing its divergence, simply replacing the charge density with $\nabla \cdot \mathbf{E}$ where needed. As demonstrated later and from extensive testing (not part of this work), we have not found any appreciable evidence of loss of accuracy or stability. Similar conclusions have been reported by [Bucciantini & Del Zanna \(2013\)](#); [Del Zanna et al. \(2016\)](#); [Tomei et al. \(2020\)](#).

While 2nd-order numerical schemes already provide an effective tool for solving such equations, higher-order methods can play a crucial role in the context of Res-RMHD simulations. An increase in overall accuracy and convergence order of the numerical integration, in fact, can significantly decrease the numerical dissipation associated to the scheme's discretization errors. The benefits of such improvements are twofold. On the one hand, higher-order schemes can generally lead to higher computational efficiencies, thus decreasing the computational time required to achieve a given accuracy ([Berta et al. 2024](#)). On the other hand, a decrease in numerical dissipation means that we can probe the dynamical impact of more realistic (i.e. lower) values of physical magnetic dissipation, which needs to dominate over the numerical one in any reliable Res-RMHD model ([Mattia et al. 2023](#)).

In this paper we extend the 4th-order accurate finite volume (FV) method described in [Berta et al. \(2024\)](#) (paper II henceforth) to the Res-RMHD equations. Our scheme employs pointwise WENO-Z spatial reconstruction (see paper II and the original paper by [Borges et al. 2008](#)) and either the strong stability preserving SSP3(4,3,3) IMEX Runge–Kutta of [Pareschi & Russo \(2003, 2005\)](#) or the more recent IMEX additive Runge-Kutta scheme ARK4(3)7L[2]SA₁ by [Kennedy & Carpenter \(2019\)](#) to achieve, respectively, 3rd- or 4th-order accuracy in time. We refer to [Carpenter et al. \(2005\)](#); [Conde et al. \(2017\)](#); [Boscheri & Pareschi \(2021\)](#) for other IMEX schemes of high order. Note that, the use of pointwise spatial reconstructions is indeed crucial to achieve accuracy beyond second order when evaluating the implicit stiff source terms within the IMEX formulation, as discussed recently in [Boscarino et al. \(2018\)](#).

The rest of the paper is structured as follows. In §2, we review the fundamental equations of Res-RMHD framework. In §3 our 4th-order FV-CT method is illustrated and in §4 we assess the robustness of the algorithm through extensive numerical benchmarking. Results are summarized in §5.

2 RESISTIVE RELATIVISTIC MHD EQUATIONS

When dealing with relativistic plasmas, it is convenient to start from the appropriate set of covariant equations. In the (single fluid) MHD approximation, these consist of the Maxwell equations

$$\nabla_\mu F^{\mu\nu} = -J^\nu, \quad \nabla_\mu F^{*\mu\nu} = 0, \quad (1)$$

where $F^{\mu\nu}$, $F^{*\mu\nu}$, J^μ are, respectively, the Faraday tensor, its dual, the four-current density, and in the conservation laws for mass and total (gas and electromagnetic fields) energy-momentum

$$\nabla_\mu(\rho u^\mu) = 0, \quad \nabla_\mu T^{\mu\nu} \equiv \nabla_\mu(T_{\text{gas}}^{\mu\nu} + T_{\text{em}}^{\mu\nu}) = 0, \quad (2)$$

where ρ is the rest mass density, u^μ is the four-velocity of the fluid, and $T^{\mu\nu}$ is the total energy-momentum tensor. The two contributions are, respectively

$$\begin{aligned} T_{\text{gas}}^{\mu\nu} &= \rho h u^\mu u^\nu + p g^{\mu\nu}, \\ T_{\text{em}}^{\mu\nu} &= F^\mu_\lambda F^{\nu\lambda} - \frac{1}{4}(F_{\lambda\kappa} F^{\lambda\kappa}) g^{\mu\nu}, \end{aligned} \quad (3)$$

where h , ε , p are respectively the gas specific enthalpy, energy density and pressure, as measured in the fluid rest frame and related by $\rho h = \varepsilon + p$. These thermodynamic quantities must be also connected by an *Equation of State* (EoS), for instance, given in the form $h = h(\rho, p)$.

It is convenient to express the Faraday tensor and its dual in terms of the four-velocity and the magnetic b^μ and electric e^μ fields measured in the fluid rest frame

$$\begin{aligned} F^{\mu\nu} &= u^\mu e^\nu - u^\nu e^\mu + \epsilon^{\mu\nu\lambda\kappa} b_\lambda u_\kappa, \\ F^{*\mu\nu} &= u^\mu b^\nu - u^\nu b^\mu - \epsilon^{\mu\nu\lambda\kappa} e_\lambda u_\kappa, \end{aligned} \quad (4)$$

where $\epsilon^{\mu\nu\lambda\kappa}$ represents the Levi-Civita pseudo-tensor. Ideal relativistic MHD is obtained by assuming a vanishing electric field in the frame comoving with the fluid, while in the resistive case we will assume a simple Ohmic relation

$$e^\mu = \eta j^\mu, \quad (5)$$

where $j^\mu = J^\mu + (J^\nu u_\nu)u^\mu$ is the current density measured in the fluid frame and η is the resistivity coefficient, supposed to be a scalar for the sake of simplicity.

Assuming from now on a Minkowski flat spacetime and splitting time and space, it is convenient to write the fluid velocity as

$$u^\mu = (\sqrt{1+u^2}, \mathbf{u}) \equiv (\gamma, \gamma\mathbf{v}), \quad (6)$$

where \mathbf{v} is the usual three-dimensional velocity of the fluid measured in the laboratory frame and γ the associated Lorentz factor, while the electromagnetic fields can be split as

$$\begin{aligned} e^\mu &= (\mathbf{u} \cdot \mathbf{E}, \gamma \mathbf{E} + \mathbf{u} \times \mathbf{B}), \\ b^\mu &= (\mathbf{u} \cdot \mathbf{B}, \gamma \mathbf{B} - \mathbf{u} \times \mathbf{E}), \end{aligned} \quad (7)$$

where \mathbf{E} and \mathbf{B} are the usual electric and magnetic fields measured in the laboratory frame. The four-current can be also split

$$J^\mu = (q, \mathbf{J}) = (q, q\mathbf{v} + \eta^{-1} \tilde{\mathbf{E}}), \quad (8)$$

in which q is the charge density measured in the laboratory frame and \mathbf{J} the spatial current density, with

$$\tilde{\mathbf{E}} \equiv \gamma \mathbf{E} + \mathbf{u} \times \mathbf{B} - (\mathbf{E} \cdot \mathbf{u})\mathbf{v} \Rightarrow \tilde{\mathbf{E}} = \eta(\mathbf{J} - q\mathbf{v}), \quad (9)$$

where Eqns. (5) and (7) has been used. Given the above spatial vectors, Maxwell's system is written in the usual way, a couple of evolutionary equations

$$\frac{\partial \mathbf{B}}{\partial t} + \nabla \times \mathbf{E} = 0, \quad \frac{\partial \mathbf{E}}{\partial t} - \nabla \times \mathbf{B} = -\mathbf{J}, \quad (10)$$

and a couple of non-evolutionary constraints

$$\nabla \cdot \mathbf{B} = 0, \quad \nabla \cdot \mathbf{E} = q, \quad (11)$$

and we use the latter, Gauss's law, to define the charge density q .

The final system of resistive relativistic magnetohydrodynamics (RRMHD) is retrieved by splitting the covariant equations (2), and by the first couple of Maxwell's equations (10). We obtain 11 evolution equations which may be written in the form of a set of conservation laws with source terms

$$\frac{\partial U}{\partial t} = -\nabla \cdot \mathbf{F}(U) + S_e(U) + S(U), \quad (12)$$

where

$$U = \begin{pmatrix} D \\ m_i \\ \mathcal{E} \\ B_i \\ E_i \end{pmatrix}, \quad \mathbf{F}_j = \begin{pmatrix} \rho u_j \\ \rho h u_i u_j - E_i E_j - B_i B_j + p_{\text{tot}} \delta_{ij} \\ m_j \\ \varepsilon^{ijk} E_k \\ -\varepsilon^{ijk} B_k \end{pmatrix}, \quad (13)$$

with ε^{ijk} is the three-dimensional Levi-Civita symbol. Here the mass density $D = \rho\gamma$, the total momentum density $\mathbf{m} = Dh\mathbf{u} + \mathbf{E} \times \mathbf{B}$, and the total energy density $\mathcal{E} = Dh\gamma - p + u_{\text{em}}$ (all measured in the laboratory frame) are the so-called *conserved* variables, where $u_{\text{em}} = (E^2 + B^2)/2$ is the electromagnetic energy density, and $p_{\text{tot}} = p + u_{\text{em}}$ is the total pressure. These variables are expressed in terms of the *primitive* variables ρ , \mathbf{v} , and p . Notice that the electric and magnetic fields \mathbf{E} and \mathbf{B} act as both conserved and primitive variables.

The source term is non-zero only in the equation for \mathbf{E} and it contains the spatial current density \mathbf{J} in Eq. (8). This is split, for computational purposes, into standard and *stiff* ($\propto 1/\eta$) contributions, so that the source terms S_e and S in Eq. (12) are given by

$$S_e = \begin{pmatrix} 0_{\times 8} \\ -q\mathbf{v}_i \end{pmatrix}, \quad S = \frac{1}{\eta} \begin{pmatrix} 0_{\times 8} \\ -\tilde{\mathbf{E}}_i \end{pmatrix}, \quad (14)$$

where $\tilde{\mathbf{E}}$ is defined in Eq. (9). Numerical stiffness is obviously given by the fact that the resistivity coefficient η is negligible in real astrophysical plasmas, and finite but very small in computational applications, so the term S can be very large and special care should be adopted for the evolution of the electric field (the terms R and S will be treated differently in the numerical time evolution of U).

We recall that in ideal MHD, that is assuming the limit $\eta \rightarrow 0$, this latter equation is not evolved at all, the current does not need to be computed, and the electric field is a derived quantity, simply given by $\mathbf{E} = -\mathbf{v} \times \mathbf{B}$, so that $\tilde{\mathbf{E}} = 0$.

3 NUMERICAL METHOD

3.1 Basic discretization

We employ a Cartesian coordinate system with axes represented by the unit vectors $\hat{\mathbf{e}}_x = (1, 0, 0)$, $\hat{\mathbf{e}}_y = (0, 1, 0)$ and $\hat{\mathbf{e}}_z = (0, 0, 1)$, uniformly discretized into a regular mesh with coordinate spacing Δx , Δy and Δz . We will frequently use the notation $\mathbf{c} = (i, j, k)$ as a short-hand to identify a single computational cell centered at (x_i, y_j, z_k) and delimited by the six interfaces orthogonal to the coordinate axis centered, respectively, at $(x_{i\pm\frac{1}{2}}, y_j, z_k)$, $(x_i, y_{j\pm\frac{1}{2}}, z_k)$, and $(x_i, y_j, z_{k\pm\frac{1}{2}})$. The grid interfaces location will be short-handed with

$$\begin{aligned} \mathbf{x}_f &\equiv \left(i + \frac{1}{2}, j, k\right), \\ \mathbf{y}_f &\equiv \left(i, j + \frac{1}{2}, k\right), \\ \mathbf{z}_f &\equiv \left(i, j, k + \frac{1}{2}\right). \end{aligned} \quad (15)$$

Likewise, we define the location of the cell edges as

$$\begin{aligned} \mathbf{x}_e &\equiv \left(i, j + \frac{1}{2}, k + \frac{1}{2}\right), \\ \mathbf{y}_e &\equiv \left(i + \frac{1}{2}, j, k + \frac{1}{2}\right), \\ \mathbf{z}_e &\equiv \left(i + \frac{1}{2}, j + \frac{1}{2}, k\right). \end{aligned} \quad (16)$$

Integrating the original PDE (Eq. 12) over a cell volume for $U = \{D, \mathbf{m}, \mathcal{E}, \mathbf{E}\}$ gives the semi-discrete form

$$\frac{d\langle U \rangle_{\mathbf{c}}}{dt} = \hat{R}_{\mathbf{c}} + \langle S \rangle_{\mathbf{c}}, \quad (17)$$

where $\langle U \rangle_{\mathbf{c}}$ denotes the volume average of the corresponding conserved quantity, $\langle S \rangle_{\mathbf{c}}$ is the stiff part of the source term (second term

in Eq. 14), while

$$\begin{aligned} \hat{R}_{\mathbf{c}} = & - \left(\frac{\hat{F}_{x,x_f} - \hat{F}_{x,x_f-\hat{\mathbf{e}}_x}}{\Delta x} \right) - \left(\frac{\hat{F}_{y,y_f} - \hat{F}_{y,y_f-\hat{\mathbf{e}}_y}}{\Delta y} \right) \\ & - \left(\frac{\hat{F}_{z,z_f} - \hat{F}_{z,z_f-\hat{\mathbf{e}}_z}}{\Delta z} \right) + \langle S_e \rangle_{\mathbf{c}}, \end{aligned} \quad (18)$$

is the explicit right-hand side including surface flux contributions plus the volume average of the explicit source term S_e (first term in Eq. 14) whose only non-vanishing component is the $q\mathbf{v}$ term in the electric field update.

In Eq. (18), \hat{F}_{x,x_f} (and likewise \hat{F}_{y,y_f} and \hat{F}_{z,z_f}) represents the surface-integrated numerical flux across an x -face, i.e.:

$$\hat{F}_{x,x_f} = \frac{1}{\Delta y \Delta z} \int F_{x,x_f} dy dz, \quad (19)$$

which has to be computed with a high-order quadrature rule. Expressions for the y - and z -directions are obtained in a similar fashion.

Magnetic field variables are treated as staggered quantities and are evolved using the integral form of Faraday's law (the first in Eq. 10) and direct application of Stokes' theorem (see §2, §3 and §4 of paper II for more details). Thus, if \hat{B}_{x,x_f} , \hat{B}_{y,y_f} and \hat{B}_{z,z_f} are the surface-averaged components of \mathbf{B} lying, respectively, on the x -, y - and z -interfaces, the constrained transport (CT, see Yee 1966; Brecht et al. 1981; Evans & Hawley 1988; Balsara & Spicer 1999) algorithm entails the following discrete update:

$$\begin{aligned} \frac{d\hat{B}_{x,x_f}}{dt} &= - \left(\frac{\bar{E}_{z,z_e} - \bar{E}_{z,z_e-\hat{\mathbf{e}}_y}}{\Delta y} - \frac{\bar{E}_{y,y_e} - \bar{E}_{y,y_e-\hat{\mathbf{e}}_z}}{\Delta z} \right), \\ \frac{d\hat{B}_{y,y_f}}{dt} &= - \left(\frac{\bar{E}_{x,x_e} - \bar{E}_{x,x_e-\hat{\mathbf{e}}_z}}{\Delta z} - \frac{\bar{E}_{z,z_e} - \bar{E}_{z,z_e-\hat{\mathbf{e}}_x}}{\Delta x} \right), \\ \frac{d\hat{B}_{z,z_f}}{dt} &= - \left(\frac{\bar{E}_{y,y_e} - \bar{E}_{y,y_e-\hat{\mathbf{e}}_x}}{\Delta x} - \frac{\bar{E}_{x,x_e} - \bar{E}_{x,x_e-\hat{\mathbf{e}}_y}}{\Delta y} \right). \end{aligned} \quad (20)$$

In the previous expressions we have denoted the line-averaged electric field (electromotive force, or emf) at zone edges with \bar{E}_{x,x_e} , \bar{E}_{y,y_e} and \bar{E}_{z,z_e} . The actual computations of the emf is detailed in §3.7.

Finally, it is worth to remind that in the presented 4th-order scheme only magnetic field components are evolved as surface-average, while electric field (unlike paper I) is treated as a zone-centered variable rather than in a staggered fashion.

3.2 Temporal update

Equations (17) and (20) are evolved in time using implicit-explicit (IMEX) Runge Kutta (RK) schemes, for stiffly-accurate computations. When applied to Eq. (17), an IMEX RK scheme can be expressed following the general formulation of Ascher et al. (1997); Pareschi & Russo (2005), yielding

$$\begin{aligned} \langle U \rangle_{\mathbf{c}}^{(k)} &= \langle U \rangle_{\mathbf{c}}^n + \Delta t \sum_{j=1}^{k-1} \tilde{a}_{kj} \hat{R}_{\mathbf{c}} + \Delta t \sum_{j=1}^k a_{kj} \langle S \rangle_{\mathbf{c}}^{(j)}, \\ \langle U \rangle_{\mathbf{c}}^{n+1} &= \langle U \rangle_{\mathbf{c}}^n + \Delta t \sum_{j=1}^{\nu} \tilde{w}_j \hat{R}_{\mathbf{c}}^{(j)} + \Delta t \sum_{j=1}^{\nu} w_j \langle S \rangle_{\mathbf{c}}^{(j)}, \end{aligned} \quad (21)$$

where ν is the number of integration stages, \tilde{A} is a $\nu \times \nu$ lower triangular matrix ($\tilde{a}_{ij} = 0, \forall j \geq i$) enclosing the coefficients of the explicit right-hand side $\hat{R}_{\mathbf{c}}$ (Eq. 18 or the right-hand side of Eq. 20),

while $A = (a_{ij})$ is also a $\nu \times \nu$ matrix including the coefficients for the implicit part of the right-hand side, $S^{(j)}$. We recall that the use of a diagonally implicit Runge-Kutta (DIRK) solver guarantees an explicit evaluation of the non-stiff terms and implicit evaluation only for the diagonally stiff terms.

The final stage is always explicit and it is expressed in terms of the coefficient vectors $\tilde{w} = (\tilde{w}_1, \dots, \tilde{w}_\nu)^T$, and $w = (w_1, \dots, w_\nu)^T$. IMEX Runge-Kutta schemes are conveniently represented with a double tableau in the usual Butcher notation,

$$\begin{array}{c|c} \tilde{c} & \tilde{A} \\ \hline & \tilde{w}^T \end{array} \quad \begin{array}{c|c} c & A \\ \hline & w^T \end{array} \quad (22)$$

where the coefficients \tilde{c} and c refer to the treatment of non-autonomous systems and are defined as

$$\tilde{c}_i = \sum_{j=1}^{i-1} \tilde{a}_{ij}, \quad c_i = \sum_{j=1}^i a_{ij}. \quad (23)$$

In this paper we consider two IMEX time-stepping methods: i) the 3rd-order accurate IMEX Strong Stability Preserving SSP3(4,3,3) scheme of [Pareschi & Russo \(2005\)](#) (with 4 implicit, and 3 explicit stages) and ii) the 4th-order IMEX ARK4(3)7L[2]SA₁ of [Kennedy & Carpenter \(2019\)](#) (ARK4 hereafter) which is L-stable, stiffly accurate (SA) with 7 stages. The explicit coefficients of both methods can be found in [Appendix A](#).

From an algorithmic viewpoint, during the explicit-implicit update we found more convenient to separate the explicit contributions (acting on volume averages) from the implicit part which, in our formulation, will be operated on pointwise values. For the generic k -th stage in Eq. (21), we therefore act as follows:

$$\langle U \rangle_{\mathbf{c}}^{(k*)} = \langle U \rangle_{\mathbf{c}}^n + \Delta t \sum_{j=1}^{k-1} \left(\tilde{a}_{kj} \hat{R}_{\mathbf{c}} + a_{kj} \langle S \rangle_{\mathbf{c}}^{(j)} \right), \quad (24)$$

$$U_{\mathbf{c}}^{(k)} = U_{\mathbf{c}}^{(k*)} + \Delta t a_{kk} S_{\mathbf{c}}^{(k)}.$$

where the former step (k^*) is explicit while the latter (k) is implicit. The algorithm is summarized in [§3.10](#).

3.3 Point value recovery of primitive variables

Our algorithm starts with the zone-averaged value of the solution $\langle U \rangle_{\mathbf{c}}$ inside a cell and the face-averaged values of the staggered components of the magnetic field, $\hat{\mathbf{B}}$. At the very first step, we require the point value of the solution at the cell-center. Following paper II, this operation may be carried out using the Laplacian operator,

$$U_{\mathbf{c}} = \left(1 - \frac{\Delta}{24} \right) \langle U \rangle_{\mathbf{c}} + \mathcal{O}(h^4), \quad (25)$$

where Δ is the Laplacian operator first introduced in the context of high-order methods by [McCorquodale & Colella \(2011\)](#), i.e.

$$\Delta \langle U \rangle_{\mathbf{c}} \equiv (\Delta^x + \Delta^y + \Delta^z) \langle U \rangle_{\mathbf{c}}, \quad (26)$$

where, e.g.,

$$\Delta^x \langle U \rangle_{\mathbf{c}} = (\langle U \rangle_{\mathbf{c}-\hat{\mathbf{e}}_x} - 2 \langle U \rangle_{\mathbf{c}} + \langle U \rangle_{\mathbf{c}+\hat{\mathbf{e}}_x}), \quad (27)$$

and similarly of the y - and z -directions. Note that this step applies only to cell-centered quantities, i.e., lab density, momentum, energy and electric fields. For the magnetic field, instead, one has to first recover its point values at face centers using only the transverse

Laplacian, so that

$$\begin{aligned} B_{x,x_f} &= \left(1 - \frac{\Delta^y + \Delta^z}{24} \right) \hat{B}_{x,x_f}, \\ B_{y,y_f} &= \left(1 - \frac{\Delta^z + \Delta^x}{24} \right) \hat{B}_{y,y_f}, \\ B_{z,z_f} &= \left(1 - \frac{\Delta^x + \Delta^y}{24} \right) \hat{B}_{z,z_f}. \end{aligned} \quad (28)$$

Then, following [Felker & Stone \(2018\)](#), the pointwise value of the magnetic field at the cell center is obtained using an unlimited high-order interpolation, i.e.:

$$\begin{aligned} B_{x,c} &= -\frac{1}{16} (B_{x,x_f+\hat{\mathbf{e}}_x} + B_{x,x_f-2\hat{\mathbf{e}}_x}) + \frac{9}{16} (B_{x,x_f} + B_{x,x_f-\hat{\mathbf{e}}_x}), \\ B_{y,c} &= -\frac{1}{16} (B_{y,y_f+\hat{\mathbf{e}}_y} + B_{y,y_f-2\hat{\mathbf{e}}_y}) + \frac{9}{16} (B_{y,y_f} + B_{y,y_f-\hat{\mathbf{e}}_y}), \\ B_{z,c} &= -\frac{1}{16} (B_{z,z_f+\hat{\mathbf{e}}_z} + B_{z,z_f-2\hat{\mathbf{e}}_z}) + \frac{9}{16} (B_{z,z_f} + B_{z,z_f-\hat{\mathbf{e}}_z}). \end{aligned} \quad (29)$$

Now that all conservative variables are available at zone centers as point values, we convert them to primitive variables, i.e., $V_{\mathbf{c}} = \mathcal{V}(U_{\mathbf{c}})$. The conversion between conservative and primitive variables cannot be written in closed analytical form as it requires the inversion of a nonlinear function. Differently from paper I, here we prefer to follow an approach similar to that of [Palenzuela et al. \(2009\)](#), which consists of subtracting the electromagnetic contributions from momentum and energy densities and then resorting to a standard relativistic hydro inversion scheme to find the pressure. In our implementation, we employ the root solver of [Mignone et al. \(2005\)](#) (see also [§2](#) in [Mignone & Bodo 2005](#)) that can be extended to different equations of state.

Note that Eq. (25) may produce unphysical states in presence of sharp gradients and in regions of rapidly changing profiles. A limiting strategy to identify troubled cells is indeed necessary before operating any conversion operation to maintain numerical stability. We discuss our fallback approach in [§3.9](#) of the present paper, while the reader may consult [§3.4](#) of paper II for a full description.

3.4 Implicit update of pointwise quantities

During the implicit part of our update (see the second equation in [24](#)), we operate directly on the point value of the electric field vector:

$$\mathbf{E} = \mathbf{E}^* - \frac{1}{\tilde{\eta}} [\gamma \mathbf{E} + \mathbf{u} \times \mathbf{B} - (\mathbf{E} \cdot \mathbf{u}) \mathbf{v}], \quad (30)$$

where, by analogy Eq. (24), we identify $\mathbf{E}^* \equiv \mathbf{E}^{(k*)}$ (available from the last explicit stage) and $\tilde{\eta} = \eta / (a_{kk} \Delta t)$ which is now a non-dimensional quantity. The previous equation provides a relation between the electric field \mathbf{E} and the four-velocity \mathbf{u} . Using

$$\mathbf{E} \cdot \mathbf{u} = \frac{\tilde{\eta} \gamma}{1 + \tilde{\eta} \gamma} (\mathbf{E}^* \cdot \mathbf{u}), \quad (31)$$

we can re-write Eq. (30) as an explicit function $\mathbf{E} \equiv \mathbf{E}(\mathbf{u})$:

$$(\tilde{\eta} + \gamma) \mathbf{E}(\mathbf{u}) = \tilde{\eta} \mathbf{E}^* - \mathbf{u} \times \mathbf{B} + \frac{\tilde{\eta}}{1 + \tilde{\eta} \gamma} (\mathbf{E}^* \cdot \mathbf{u}) \mathbf{u}, \quad (32)$$

where $\gamma = \sqrt{1 + u^2}$.

Note that the four-velocity is not a conservative variable and it must be derived from the set of conserved variables U . Since momentum

does not change during the implicit step, we use the implicit relation

$$\mathbf{f}(\mathbf{u}) = \mathbf{m} - \left(Dh(\mathbf{u})\mathbf{u} + \mathbf{E}(\mathbf{u}) \times \mathbf{B} \right) = \mathbf{0}. \quad (33)$$

to derive \mathbf{u} , ad in paper I. Note also that D and \mathbf{B} are held constant during this step. Following [Bucciantini & Del Zanna \(2013\)](#), we adopt a Newton-Broyden root-finding method to derive the four-velocity (and the other primitive variables) from the set of conserved variables. Additionally, we refer the reader to [Mattia et al. \(2023\)](#) for a generalization of the Taub equation of state ([Mignone et al. 2005](#)) and to [Tomei et al. \(2020\)](#) for a more comprehensive treatment of the dynamo term in Ohm's law along with for any spacetime metric in general relativity. The iterative multi-dimensional Newton-Broyden algorithm can be sketched as follows:

- (i) At the beginning of any step $\kappa = 0, 1, 2, \dots$, use Eq. (32) to obtain $\mathbf{E} = \mathbf{E}(\mathbf{u})$. When $\kappa = 0$, an initial guess for the four-velocity is needed: if $\tilde{\eta} > 1$, employ the value provided at the current time level, otherwise reckon that obtained from the ideal RMHD equations.

- (ii) Given $\mathbf{u}^{(\kappa)}$ and $\mathbf{E}^{(\kappa)}$, compute $\mathbf{f}^{(\kappa)} \equiv \mathbf{f}(\mathbf{u}^{(\kappa)})$ from the conservation of the total momentum density

$$\mathbf{f}^{(\kappa)} = \mathbf{m} - \left[Dh(\mathbf{u})\mathbf{u} + \mathbf{E}(\mathbf{u}) \times \mathbf{B} \right]^{(\kappa)}. \quad (34)$$

Notice that the laboratory density, magnetic field, total energy and the conserved momentum remain constant during this iteration scheme. Eq. (34) represents a set of three nonlinear equations to be solved for $\mathbf{u}^{(\kappa)}$. Thermodynamics quantities are also written as functions of the four-velocity; for an ideal gas law one finds

$$h(\mathbf{u}) = 1 + \Gamma_1 \frac{p\gamma}{D}, \quad (35)$$

with $\Gamma_1 = \Gamma/(\Gamma - 1)$ ($\Gamma = 4/3$ for relativistically hot plasmas), and, from the conservation of the total energy, the pressure is derived as

$$p(\mathbf{u}) = \frac{\mathcal{E} - D\gamma - (E^2 + B^2)/2}{\Gamma_1\gamma^2 - 1}. \quad (36)$$

- (iii) Using the Jacobian $\mathbf{J} = \partial\mathbf{f}/\partial\mathbf{u}$, obtain an improved guess of the four-velocity through

$$\mathbf{u}^{(\kappa+1)} = \mathbf{u}^{(\kappa)} - \left(\mathbf{J}^{(\kappa)} \right)^{-1} \mathbf{f}^{(\kappa)}, \quad (37)$$

with the explicit form of the Jacobian being

$$J_{ij} \equiv \frac{\partial f_i}{\partial u_j} = -Dh \delta_{ij} - D u_i \frac{\partial h}{\partial u_j} - \epsilon_{ilm} \frac{\partial E_l}{\partial u_j} B_m. \quad (38)$$

The derivatives of h and \mathbf{E} are given by

$$D \frac{\partial h}{\partial u^j} = -\frac{\Gamma_1}{\gamma^2 \Gamma_1 - 1} \left[(\gamma h D + p) v_j + \gamma E_i \frac{\partial E_i}{\partial u_j} \right], \quad (39)$$

given the relation $\partial\gamma/\partial u_j = u_j/\gamma = v_j$, and, from Eq. (32), by

$$\begin{aligned} (\tilde{\eta} + \gamma) \frac{\partial E_i}{\partial u_j} &= -E_i v_j - \epsilon_{ijk} B_k \\ &+ \frac{\tilde{\eta}}{1 + \tilde{\eta}\gamma} \left[u_i E_j^* + (\mathbf{E}^* \cdot \mathbf{u}) \left(\delta_{ij} - \frac{\tilde{\eta}}{1 + \tilde{\eta}\gamma} u_i v_j \right) \right], \end{aligned} \quad (40)$$

which can be also compared to the Jacobian presented in [Tomei et al. \(2020\)](#) (for a vanishing dynamo coefficient $\xi = 0$).

- (iv) Exit the iteration cycle if the error is less than some prescribed accuracy $|\mathbf{f}^{(\kappa)}| < \epsilon$, otherwise go back to step (i) and let $\kappa \rightarrow \kappa + 1$. For standard applications, our algorithm converges in 2–5 iterations given a relative tolerance of 10^{-11} .

The above procedure is to be implemented at the beginning of all IMEX substeps at cell centers using pointwise quantities. Furthermore, it automatically operates the conversion from conservative to primitive variables, which are then readily available for reconstruction at cell interfaces and flux computation. For this reason, this procedure must be extended also to a layer of ghost zones (e.g., 3 for a 5-point stencil reconstruction) in order to avoid extra communication at the end of the implicit step.

3.5 Point value reconstruction of primitive variables

Reconstruction at interfaces is operated directly on the function point values rather than on the one-dimensional average quantities as firstly introduced by paper II. In the following paragraphs, we summarize the pointwise 5th-order weighted essentially non-oscillatory scheme of Borges et al. (WENO-Z, see [Borges et al. 2008](#)).

The interface value presented in Eq. (23) of paper II at $x = x_{i+\frac{1}{2}}$ is computed as the convex combination of 3rd-order accurate interface values built on the three possible three-point sub-stencils $\{i-2, i-1, i\}$, $\{i-1, i, i+1\}$, and $\{i, i+1, i+2\}$, i.e.

$$\begin{aligned} V_{i+\frac{1}{2}}^L &= \omega_0 \frac{3V_{i-2} - 10V_{i-1} + 15V_i}{8} \\ &+ \omega_1 \frac{-V_{i-1} + 6V_i + 3V_{i+1}}{8} \\ &+ \omega_2 \frac{3V_i + 6V_{i+1} - V_{i+2}}{8}, \end{aligned} \quad (41)$$

with $\{V_{i\pm 2}, V_{i\pm 1}, V_i\}$ point values. The weights ω_l , for $l = \{0, 1, 2\}$, are defined as

$$\omega_l = \frac{\alpha_l}{\sum_m \alpha_m}, \quad \alpha_l = d_l \left(1 + \frac{|\beta_0 - \beta_2|}{\beta_l + \epsilon} \right). \quad (42)$$

Here $d_l = \{d_0 = 1/16, d_1 = 5/8, d_2 = 5/16\}$ denotes the optimal weights that reckon the 5th-order accurate approximation of Eq. (23) of paper II, $\epsilon = 10^{-40}$ is a small number avoiding division by zero and β_l are the smoothness indicators (Eq. 26 of paper II). A detailed description of pointwise reconstructions is presented in §3 of paper II.

3.6 Riemann solver & flux computation

The integrand in Eq. (19) is approximated by means of a Riemann solver which, following the traditional formalism of FV Godunov schemes, returns a stable and consistent numerical flux as a function of L/R interface states obtained in the previous section. We will employ the MLLC solver described in paper I, which considers Maxwell's and gasdynamics equations decoupled during this step. This leads to i) a pair of outermost electromagnetic waves leading to jumps in \mathbf{E} , \mathbf{B} (and therefore total momentum and energy) and ii) an inner wave fan including two hydrodynamics shocks enclosing a contact wave.

At the practical level, we first obtain the transverse components of \mathbf{E} and \mathbf{B} using Maxwell's jump conditions. Specializing at an

x -interface:

$$\begin{aligned}\tilde{B}_y &= \frac{B_{y,L} + B_{y,R}}{2} + \frac{E_{z,R} - E_{z,L}}{2} \\ \tilde{B}_z &= \frac{B_{z,L} + B_{z,R}}{2} - \frac{E_{y,R} - E_{y,L}}{2} \\ \tilde{E}_y &= \frac{E_{y,L} + E_{y,R}}{2} - \frac{B_{z,R} - B_{z,L}}{2} \\ \tilde{E}_z &= \frac{E_{z,L} + E_{z,R}}{2} + \frac{B_{y,R} - B_{y,L}}{2}.\end{aligned}\quad (43)$$

Normal components (B_x and E_x) remain continuous.

Next, we compute the hydrodynamics flux \mathcal{H}^* using the HLLC relativistic solver of [Mignone & Bodo \(2005\)](#):

$$\mathcal{H}^* = \begin{cases} \mathcal{H}_L & \text{if } \lambda_L > 0, \\ \mathcal{H}_L + \lambda_L (\mathcal{W}_L^* - \mathcal{W}_L) & \text{if } \lambda_L < 0 < \lambda^*, \\ \mathcal{H}_R + \lambda_R (\mathcal{W}_R^* - \mathcal{W}_R) & \text{if } \lambda^* < 0 < \lambda_R, \\ \mathcal{H}_R & \text{if } \lambda_R < 0, \end{cases}\quad (44)$$

where $\mathcal{H}_S = (D, Q_k v_x + p \delta_{kx}, Q_x)_S$, $S = L, R$ denotes the left or right states, $k = x, y, z$ is the spatial component, $\mathcal{W}_S = (D, Q_k, \mathcal{E}_h)_S$, $\mathcal{E}_h = w\gamma^2 - p$ is the gas energy, and $Q_k = w\gamma^2 v_k$ is the k -th component of the gas momentum. The wave speeds $\lambda_{L/R}$ are estimated from the fastest and slowest speeds as in [Mignone & Bodo \(2005\)](#). The states in the star region enclosing the contact mode are obtained as

$$\mathcal{W}_S^* = \frac{1}{\lambda_S - \lambda^*} \begin{pmatrix} D(\lambda - v_x) \\ Q_k(\lambda - v_x) + (p^* - p)\delta_{kx} \\ E(\lambda - v_x) + p^*\lambda^* - p v_x \end{pmatrix}_S \quad (45)$$

for $S = L, R$ and the speed of the contact mode $\lambda_L^* = \lambda_R^* = \lambda^*$ is found from the negative branch of the quadratic equation

$$\mathcal{H}_{[\mathcal{E}]}^{\text{hll}} (\lambda^*)^2 - (\mathcal{W}_{[\mathcal{E}_h]}^{\text{hll}} + \mathcal{H}_{[Q_x]}^{\text{hll}}) \lambda^* + \mathcal{W}_{[Q_x]}^{\text{hll}} = 0. \quad (46)$$

Here the subscript $[\cdot]$ picks a specific component of the array, while $p^* = \mathcal{H}_{[Q_x]}^{\text{hll}} - \lambda^* \mathcal{H}_{[\mathcal{E}_h]}^{\text{hll}}$ is the pressure in the star region, and the superscript hll indicates the HLL-average state (see Eq. 73 and 74 in paper I). Putting all together, we retrieve the final flux:

$$\mathcal{F}_{x,x_f} = \begin{pmatrix} \mathcal{H}^* \\ 0_{\times 6} \end{pmatrix} + \begin{pmatrix} 0 \\ \hat{\mathbf{e}}_x \cdot \tilde{\mathbf{T}} \\ \hat{\mathbf{e}}_x \cdot (\tilde{\mathbf{E}} \times \tilde{\mathbf{B}}) \\ \hat{\mathbf{e}}_x \times \tilde{\mathbf{E}} \\ -\hat{\mathbf{e}}_x \times \tilde{\mathbf{B}} \end{pmatrix}. \quad (47)$$

A similar procedure is followed to calculate the y - and z -interface fluxes.

Finally, 4th-order accuracy at zone interfaces is ensured by computing the surface-averaged flux through

$$\hat{F}_{x,x_f} = \left(1 + \frac{\Delta^y + \Delta^z}{24} \right) \mathcal{F}_{x,x_f}. \quad (48)$$

where $\Delta^{y,z}$ have been defined in Eq. (26) and Eq. (27). Note that the fluxes are used to update density, momentum, energy and electric fields. Magnetic fields, instead, are advanced in a separate step using the constrained transport formalism (see §3.7).

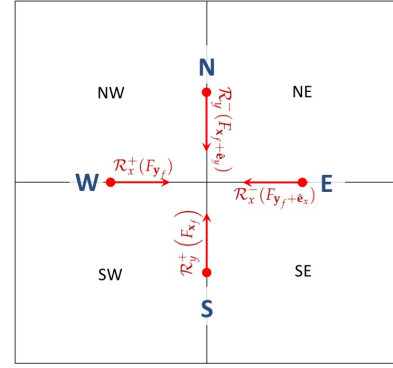


Figure 1. Top view of the intersection between four neighbor zones in the xy plane. N, S, E, and W indicate the four cardinal directions with respect to the zone edge (here represented by the intersection between four neighbor zones), $\mathcal{R}_x(F_{y_f})$ and $\mathcal{R}_y(F_{x_f})$ are 1-D reconstruction operators applied to each zone face, see Eq. (49) and (51).

3.7 Constrained Transport update

During the staggered update, we evolve the face-averaged components of magnetic fields using Eq. (20). In order to retain 4th-order accuracy we follow the steps already illustrated by paper II. In what follows, we recap the procedure.

First, one needs to reconstruct the L/R transverse electric field components from the four faces sharing the same edge to that edge. With reference to Fig. 1, which shows a top view of a z -edge in the xy plane, this entails a reconstruction of the four adjacent values of E_z (available at the x - and y -face centers) along the transverse directions (y and x , respectively) to obtain four discontinuous values coming up at $\mathbf{z}_e \equiv (i + \frac{1}{2}, j + \frac{1}{2}, k)$:

$$\begin{aligned} E_{z,z_e}^S &= \mathcal{R}_y^+(E_{z,x_f}), & E_{z,z_e}^N &= \mathcal{R}_y^-(E_{z,x_f+\hat{\mathbf{e}}_y}), \\ E_{z,z_e}^W &= \mathcal{R}_x^+(E_{z,y_f}), & E_{z,z_e}^E &= \mathcal{R}_x^-(E_{z,y_f+\hat{\mathbf{e}}_x}), \end{aligned}\quad (49)$$

where the four cardinal directions in square brackets are referred to the edge location \mathbf{z}_e . For convenience, only one component per face has to be reconstructed¹:

$$E_{z,x_f} = \frac{E_{z,x_f}^L + E_{z,x_f}^R}{2}. \quad (50)$$

In 3D, one has to repeat the reconstruction (Eq. 49) for E_{x,y_f} and E_{x,z_f} , respectively, along the z - and y -direction to \mathbf{x}_e and also for E_{y,x_f} and E_{y,z_f} along the z - and x -directions to \mathbf{y}_e .

Next, we also reconstruct the face-centered point values of the normal components of the magnetic field towards the same edge:

$$\begin{aligned} B_{x,z_e}^S &= \mathcal{R}_y^+(B_{x,x_f}), & B_{x,z_e}^N &= \mathcal{R}_y^-(B_{x,x_f+\hat{\mathbf{e}}_y}), \\ B_{y,z_e}^W &= \mathcal{R}_x^+(B_{y,y_f}), & B_{y,z_e}^E &= \mathcal{R}_x^-(B_{y,y_f+\hat{\mathbf{e}}_x}). \end{aligned}\quad (51)$$

Eqns (49) and (51) allow us to obtain the edge-centered point value of the upwind electric field, using the CT-Maxwell averaging scheme (see §3.4.2 of paper I):

$$E_{z,z_e} = \left[\frac{E_z^N + E_z^S + E_z^W + E_z^E}{4} + \frac{B_y^E - B_y^W}{2} - \frac{B_x^N - B_x^S}{2} \right]_{\mathbf{z}_e} \quad (52)$$

¹ The approach followed here differs from the one employed in paper I, where the reconstruction is performed from the cell center using linear interpolation. Also, a typo is present in Eq. (48) of paper I, since the arithmetic average operator $\langle \cdot \rangle_z$ is not needed.

Similar expressions hold for E_{x,x_e} and E_{y,y_e} by suitable index permutation.

Finally, we obtain the electromotive force (that is, the averaged line-integral of the electric field needed in the discrete version of Faraday's law Eq. 20) as

$$\bar{E}_{z,z_e} = \left(1 + \frac{\Delta z}{24}\right) E_{z,z_e}. \quad (53)$$

Eqs. (51)-(53) are extended to the 3D case by suitable index permutation.

3.8 Explicit source term computation

In addition to the flux difference operator, the right-hand side (Eq. 18) requires an explicit contribution from the $q\mathbf{v}$ source term during the electric field update. To 4th-order, this term should be included as a volume average over the zone, i.e.,

$$\langle S \rangle_e = \left(1 + \frac{\Delta}{24}\right) q_c \mathbf{v}_c, \quad (54)$$

where q_c and \mathbf{v}_c are, respectively, the point values of the charge and the fluid velocity. The former can be obtained from a cell-centered discretization of $\nabla \cdot \mathbf{E}$ yielding

$$q_c = \delta_x E_x + \delta_y E_y + \delta_z E_z. \quad (55)$$

Using the point value of the electric field already at disposal during the explicit step, we approximate (to 4th-order) the x -contribution to the divergence as

$$\delta_x E_x = \frac{8(E_{x,c+\hat{e}_x} - E_{x,c-\hat{e}_x}) - (E_{x,c+2\hat{e}_x} - E_{x,c-2\hat{e}_x})}{12\Delta x}. \quad (56)$$

Contributions along the y - and z -directions are obtained in a similar way.

We point out that the employment of unlimited differences in Eq. (56) may lead to the appearance of spurious oscillations in the presence of strong gradients. This does not represent an issue for the tests presented below, but it could be further improved by including information from the reconstructed interface values (limited). We leave this investigation to a forthcoming work.

3.9 Order reduction at discontinuities

As pointed out in paper II, 4th-order accuracy cannot be maintained in proximity of discontinuous solutions or steep gradients where the function may not be differentiable. In order to detect such features we compute, at the beginning of the RK step, the derivative ratio sensor as outlined in Sec. 3.4 of paper II. The detector flags computational cells where the order of the scheme can be locally reduced (this strategy is also known as ‘‘fallback’’ process) by i) not using the Laplacian during point value recovery and flux integration (Eq. 25 and 48) and ii) switching to either 3rd-order WENO or 2nd-order linear reconstruction.

The detector employs a five-zone stencil and does not require additional ghost zones. A similar approach is also followed by Verma et al. (2019), albeit the authors make use of ‘‘global smoothness indicators’’, defined in terms of weighted averages computed from the density and the three magnetic field components.

3.10 Algorithm summary

To better outline our algorithm, let \mathcal{D} be the set of zones comprising the active computational domain (e.g. no ghost zones). Then $\mathcal{D} + 1$

denotes the set of active computational zones augmented by one layer of ghost zones. Since the last step of an IMEX-RK scheme is always explicit, our implementation can be best summarized starting from the end of the explicit stage (k^*) (first of Eq. 24) and moving on to the next, $k \rightarrow (k+1)^*$:

1. Start with the volume average of conservative variable, $\langle U \rangle_c^{(k^*)}$, defined on \mathcal{D} at the end of the more recent explicit stage.
2. Assign boundary conditions on $\langle U \rangle_c$ in the first layer of ghost zones only so that $\langle U \rangle_c$ is correctly specified on $\mathcal{D} + 1$.
3. Recover the point value of conservative (U_c) and primitive variables, $V_c = \mathcal{V}(U_c)$ (as shown in §3.3) on \mathcal{D} only.
4. Carry out the implicit update by updating V_c on \mathcal{D} as outlined in §3.4. Notice that conservative variables U_c do not change during this step, except for the electric field components.
5. Assign boundary conditions on V_c . This will define primitive variables on $\mathcal{D} + n_g$, where $n_g = 3$.
6. Using the point value of primitive variables, compute the implicit source term point value in $\mathcal{D} + 1$, that is, $S_c = S(V_c)$.
7. Compute the zone-averaged implicit source term $\langle S \rangle_c$ on \mathcal{D} using Simpson quadrature rule.
8. Achieve the explicit step by constructing the right hand side \hat{R}_c (Eq. 18) and its staggered version (right-hand side of Eq. 20):
 - Perform spatial reconstruction on primitive point value variables (§3.5);
 - Solve a Riemann problems with L/R states at zone interfaces, see §3.6;
 - Compute the surface-averaged flux using Eq. (48);
 - Compute the point value of the electric field at zone edges (Eq. 52) following the procedure outlined in §3.7;
 - Obtain the line-averaged electro-motive force through Eq. (53);
 - Compute the volume-average of the explicit source term (§3.8).
9. Complete the explicit step by obtaining the volume average conserved variables at the next RK stage, that is $\langle U \rangle_c^{(k+1)^*}$.

Note that our formulation requires two boundary calls per stage: the first one is operated on $\langle U \rangle_c$ but it extends only to one layer of ghost zones, while the second one specifies boundary values on the point value or primitive variables V_c and it extends to 3 ghost zones. Unlike previous works, our formulation does not require more than 3 ghost zones.

4 NUMERICAL BENCHMARKS

We now verify and assess the accuracy and robustness of our implementation through standard 2D and 3D reference solutions. Unless otherwise stated, we will employ the pointwise WENO-Z reconstruction (paper II) and the MLLC Riemann solver coupled with the CT-Maxwell EMF average in all test problems. By default, order reduction (see Sec. 3.9) is disabled unless otherwise stated.

Initial conditions are integrated with a 4 point Gaussian quadrature rule whenever smooth analytic functions are considered.

For quantitative purposes, we evaluate L_1 norm errors for a generic quantity Q against a reference solution Q_{ref} as $\epsilon_1(Q) = \sum_i |Q(x_i) - Q_{\text{ref}}(x_i)|/N$, where x_i is a generic point of the domain and N is the total number of grid zones.

All computations have been carried out by means of the PLUTO astrophysical code (Mignone et al. 2007, 2012), where the 4th-order resistive method has been implemented. The Courant number is set to 0.4 (in 2D) and to 0.3 for 3D calculations.

4.1 Telegraph Equation

In the fluid rest frame, the resistive RMHD equations can be employed to study the propagation of light waves in the presence of a finite conductivity, as originally presented in [Mignone et al. \(2018\)](#) and paper I. For a large plasma inertia ($\rho \rightarrow \infty$), only the Maxwell equations may be evolved in time:

$$\begin{cases} \frac{\partial \mathbf{B}}{\partial t} + \nabla \times \mathbf{E} = 0 \\ \frac{\partial \mathbf{E}}{\partial t} - \nabla \times \mathbf{B} = -\sigma \mathbf{E}. \end{cases} \quad (57)$$

Eqns. (57) admit damped propagating plane wave solutions when $\sigma < 2|k|$, where k is the wavenumber. The exact mode in one dimension is

$$\begin{aligned} \mathbf{B} &= B_1 e^{-\sigma t/2} \cos \phi(x, t) \hat{\mathbf{n}} \\ \mathbf{E} &= B_1 e^{-\sigma t/2} \left[\frac{\mu}{k} \cos \phi(x, t) + \frac{\sigma}{2k} \sin \phi(x, t) \right] \hat{\mathbf{n}} \times \hat{\mathbf{e}}_x, \end{aligned} \quad (58)$$

where $\phi(x, t) = kx - \mu t$, $\mu = (k^2 - \sigma^2/4)^{1/2}$, while B_1 is the initial perturbation amplitude. Here, in addition to paper I, we have introduced $\hat{\mathbf{n}} = (0, \cos \Theta, \sin \Theta)$ as the oscillation direction of the magnetic field in the yz plane.

Following paper I, we rotate the 1D solution by an angle α around the z -axis and consider the 2D computational domain $x' \in [0, L_x]$, $y' \in [0, L_y]$ with $L_x = 1$, $L_y = 1/2$ discretized with $N_x \times N_x/2$ zones. Solving in a 2D domain allows us to assess the correct discretization of multi-dimensional terms. Electric and magnetic field vectors in this frame (\mathbf{E}' and \mathbf{B}') are obtained through the rotation matrix

$$\{\mathbf{E}, \mathbf{B}\}' = \begin{pmatrix} \cos \alpha & -\sin \alpha & 0 \\ \sin \alpha & \cos \alpha & 0 \\ 0 & 0 & 1 \end{pmatrix} \{\mathbf{E}, \mathbf{B}\}. \quad (59)$$

The wavevector has orientation $\mathbf{k} = k_x(1, \tan \alpha, 0)$, where $k_x = 2\pi/L_x$ while $\tan \alpha = L_x/L_y = 2$. Eq. (58) with $B_1 = 1$ and $\phi(\mathbf{x}', 0) = \mathbf{k} \cdot \mathbf{x}'$ is used to initialize the electric and magnetic field. We also set density to a very large value ($\rho = 10^{12}$) while velocity are set to zero. Periodic boundary conditions are imposed everywhere.

We employ the 4th-order ARK4 IMEX scheme and run computations at different grid resolutions for exactly one wave period $T = 2\pi/\mu$ where μ is defined after Eq. (58). In Fig. 2 we plot, from left to right, the profiles of B_z' (at the resolution $N_x = 32$), the L_1 -norm errors of $\mathbf{B} \cdot \hat{\mathbf{n}}$ and $\mathbf{E} \cdot (\hat{\mathbf{n}} \times \hat{\mathbf{e}}_x)$ as a function of the grid resolution (vectors are transformed back to the 1D frame), for $\Theta = 30^\circ$ (top panels) and $\Theta = 90^\circ$ (bottom panels). Green, blue and red colors refer to computations obtained with $\sigma = 1, 10$ and 20 , respectively. In all cases we recover the expected order of accuracy (4).

4.2 Stationary Charged Vortex

We now consider an exact equilibrium solution of the full resistive RMHD equations, originally introduced in paper I. It consists of a rotating charged flow embedded in a vertical magnetic field. Assuming purely radial dependence, hydrodynamic and electromagnetic variables are best expressed in a cylindrical coordinate system (r, ϕ, z)

as

$$\begin{cases} E_r = \frac{q_0}{2} \frac{r}{r^2 + 1} \\ B_z = \frac{\sqrt{(r^2 + 1)^2 - q_0^2/4}}{r^2 + 1} \\ v_\phi = -\frac{q_0}{2} \frac{r}{\sqrt{(r^2 + 1)^2 - q_0^2/4}} \\ p = -\frac{\rho}{\Gamma_1} + \left[\frac{4r^2 + 4 - q_0^2}{(r^2 + 1)(4 - q_0^2)} \right]^{\Gamma_1/2} \left(p_0 + \frac{\rho}{\Gamma_1} \right) \\ q = \frac{q_0}{(r^2 + 1)^2}, \end{cases} \quad (60)$$

where $\Gamma_1 = \Gamma/(\Gamma - 1)$, $p_0 = 0.1$, $q_0 = 0.7$ is the charged at $r = 0$. Density is set to unity. The initial equilibrium condition given by Eq. (60) is mapped to a 2D Cartesian domain $(x, y \in [-10, 10])$ and the system is evolved until $t = 5$. Boundary conditions replicate the equilibrium solution throughout the integration. Since the equilibrium condition does not depend on the resistivity, numerical computations with different values of the resistivity η depend solely on the stability of the algorithm.

For the present purpose we have tested both the 3rd-order SSP3(4,3,3) RK-IMEX as well as the 4th-order ARK4 schemes. Results are shown in the four panels of Fig. 3. The integrity of the solution is effectively maintained. This is demonstrated by both the pressure color map (top left panel) showing also iso-contour levels of the electric field magnitude) and the 1D horizontal cuts of the charge (top right).

In the bottom left panel of Fig. 3 we plot the charge error as a function of the resistivity and compare our results with those of paper I using a 2nd-order method. Our 4th-order scheme is able to reduce the error by two orders of magnitude and we have found that both the SSP(4,3,3) and the ARK4 yield nearly identical results. However, the ARK4 method becomes unstable for $\eta \lesssim 10^{-4}$. For this reason, we plot only the results obtained with the SSP method. Overall, the charge error exhibits minimal variation over time, underscoring the stability of the algorithm for any value of the resistivity parameter in the chosen range.

In the lower right quadrant of Fig. 3, we present the L1-norm errors of gas pressure against resolution, showcasing the achievement of 4th-order accuracy for both methods. Notably, in comparison with the results presented in Paper I, both charge and pressure errors are markedly reduced, with a two-order improvement in convergence.

4.3 2D Relativistic Rotor

We propose a resistive variant of the ideal special relativistic MHD test proposed by [Del Zanna et al. \(2003\)](#), as also presented by [Dumbser & Zanotti \(2009\)](#); [Bucciantini & Del Zanna \(2013\)](#); [Miranda-Aranguren et al. \(2018\)](#); [Nakamura et al. \(2023\)](#). An overdense clump ($\rho = 10$) concentrated in a circular region ($r = 0.1$) at the center of the computational square $[-0.5, 0.5]^2$ is rapidly spinning ($\omega = 8.5$) in a uniform medium ($\rho = 1$, $p = 1$, $\Gamma = 4/3$) at rest. The vortex is embedded in a constant magnetic field $\mathbf{B} = (1, 0, 0)$ which is progressively wrapping around the spinning vortex, launching torsional Alfvén waves in the ambient fluid. At the final time ($t = 0.3$), the torsional Alfvén waves have approximately been rotated of a 90° angle, with the magnetic pressure deforming the initially circular vortex into its characteristic oval shape.

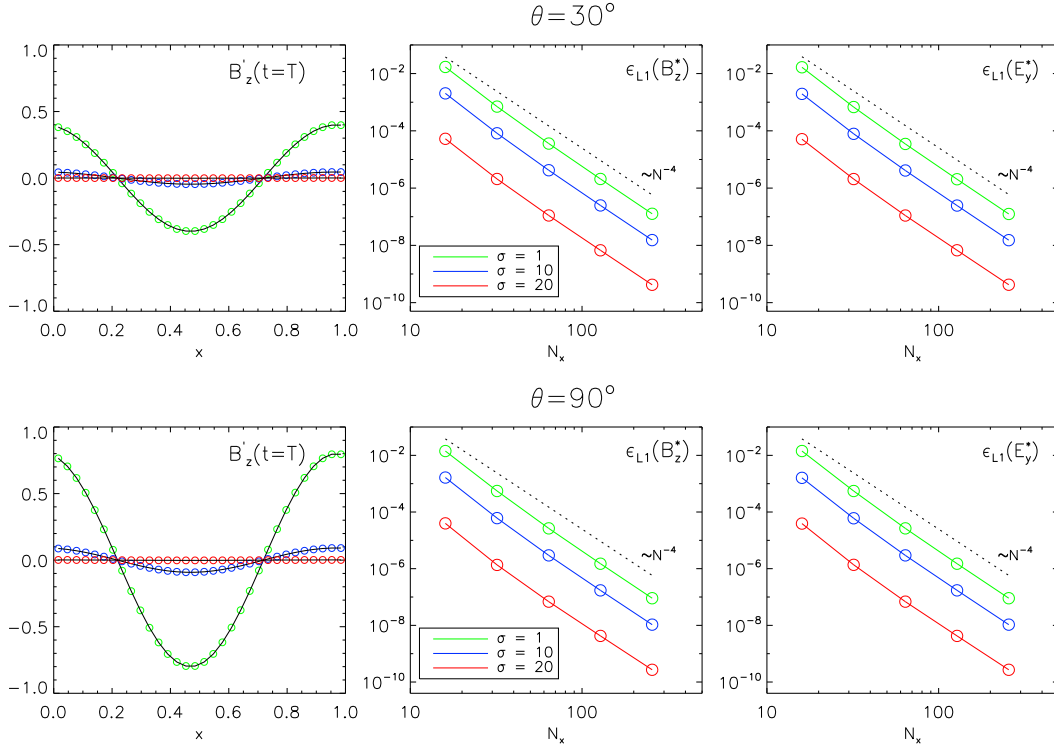


Figure 2. Numerical results of the telegraph equation test, for $\Theta = 30^\circ$ (top panels) and $\Theta = 90^\circ$ (bottom panels). Left column: 1D horizontal profiles of B'_z using different values of the $\sigma = 1, 10,$ and 20 (green, blue, and red lines respectively) for $N_x = 32$. Central and right columns: L1 norm errors of $B^* = \mathbf{B} \cdot \hat{\mathbf{n}}$ and $E^* = \mathbf{E} \cdot (\hat{\mathbf{n}} \times \hat{\mathbf{e}}_x)$ as functions of the resolution. The dashed lines give the ideal convergence slope for the 4th order.

We perform a set of 400×400 grid points simulations with increasing resistivity, from a quasi-ideal regime ($\eta = 10^{-6}, 10^{-3}$) to a fully resistive one ($\eta = 10^{-1}$). Both the SSP(4,3,3) and the ARK4 were used for this test using order reduction to WENO3. As the resistivity increases, the vortex angular momentum as well as the torsional Alfvén waves that cause the well known deformation are dissipated, leading to a more circular shape. Fig. 4 presents the snapshots of thermal pressure p (top panels), and the electric field E_z (bottom panels) at the final time $t = 0.3$. While results for SSP(4,3,3) appear essentially identical to those obtained with ARK4, only the former is able to successfully complete the integration with $\eta = 10^{-6}$, again confirming the reduced stability of the 4th-order method, which is not strong stability preserving.

It is relevant to notice how the pressure distribution is affected by the onset of spurious modes ($m = 4$) in the most resistive regime ($\eta = 10^{-1}$). This artifact results from the employment of Cartesian coordinates and it becomes more evident when using a MHLIC solver rather than a more diffusive one (with which the effect is substantially mitigated).

4.4 3D Blast Wave

The magnetized blast wave problem is used here to assess the robustness of the numerical method in handling the propagation of shock wave through magnetic field of varying strength as well as the capacity of preserving the symmetric properties of the solution. In fact, unphysical features could emerge if the divergence-free condition is not properly controlled (see, e.g. Mignone & Bodo 2006; Del Zanna et al. 2007).

Following paper I, we consider the computational domain $x, y, z \in$

$[-6, 6]$ threaded by a uniform magnetic field $\mathbf{B} = B_0 \hat{\mathbf{e}}_x$ with $B_0 = 0.1$. The plasma is initially at rest while density and pressure experience a sharp transition across a sphere of radius $r_c = 0.8$

$$\begin{pmatrix} \rho \\ p \end{pmatrix} = f_t(r) \begin{pmatrix} \rho_{\text{in}} \\ p_{\text{in}} \end{pmatrix} + (1 - f_t(r)) \begin{pmatrix} \rho_{\text{out}} \\ p_{\text{out}} \end{pmatrix} \quad (61)$$

where $f_t(r)$ is a taper (smoothing) function,

$$f_t(r) = \max \left[\min \left(\frac{e^\chi - e}{1 - e}, 1 \right), 0 \right], \quad (62)$$

with $\chi = (r - r_c)/(1 - r_c)$. Similar 3D configurations have been used by Komissarov (2007) and Dionysopoulou et al. (2013) although with larger resistivity or lower magnetic fields. The system is evolved until $t = 4$ using the SSP(4,3,3) method. We also enable order reduction to linear for this test. Zero-gradient boundary conditions apply everywhere.

Fig. 5 shows the outcomes of the simulation, presenting, in the top panel, 2D maps of the x -component of magnetic field (left), gas pressure (middle) while, in the bottom panel, electromagnetic pressure (left) and Lorentz factor (middle). In the rightmost column, we show one-dimensional profiles along the z -axis of thermal pressure (top) and Lorentz factor (bottom). As a consequence of the explosion, a swiftly advancing forward shock moves in an (almost) radial manner, while concurrently, a trailing reverse shock marks the boundary of the internal region where radial expansion occurs. Electromagnetic fields pile up in the y -direction, forming a shell characterized by elevated magnetic pressure. Gas exhibits a pronounced preference for motion along the x -direction, attaining a heightened Lorentz factor ($\gamma_{\text{max}} \approx 5.4$).

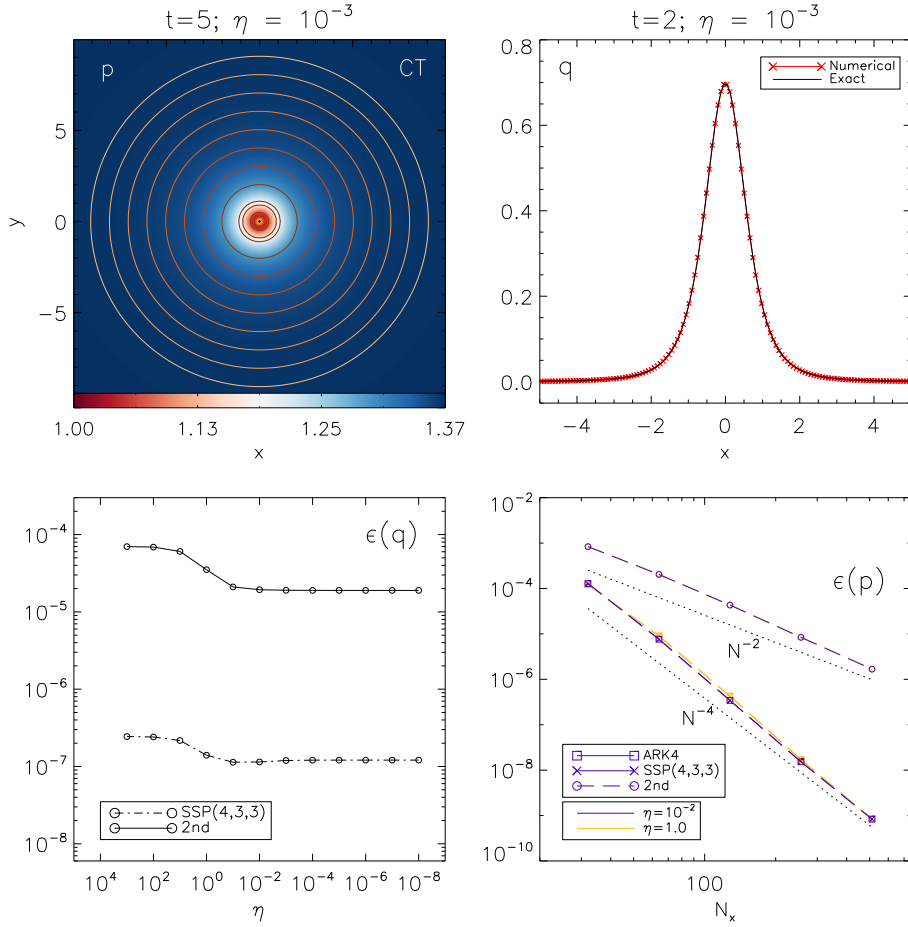


Figure 3. Numerical results of the charged vortex problem. Top-left panel: we show 8 equally spaced contour levels of E chosen as $(q_0/2)r_k/(r_k^2 + 1)$ (where $r_k = 1, \dots, 8$) overlaid on the coloured maps of pressure at $t = 5$. Resistivity is set to $\eta = 10^{-3}$ and the grid resolution is 256^2 zones. Top-right panel: 1D horizontal cuts, at $y = 0$, of charge at $t = 3$ obtained with CT. Bottom-left panel: L_1 norm errors of the charge as functions of the resistivity using CT with 256^2 zones. Bottom-right panel: L_1 norm errors of the gas pressure as functions of the resolution for the SSP(4,3,3), ARK4 and the second-order scheme. The dotted lines gives the expected second order scaling.

4.5 Tearing mode

In what follows we validate our method on the linear growth of the ideal tearing mode instability with a Harris current sheet profile, following the results presented by [Del Zanna et al. \(2016\)](#) (see also [Miranda-Aranguren et al. 2018](#), and paper I).

In this problem, a static ($v = 0$) plasma is uniformly distributed in the computational domain with constant initial density and pressure ρ_0 and p_0 . The initial magnetic field profile satisfies the force-free condition and it is given by

$$\mathbf{B} = B_0 \left[\tanh\left(\frac{x}{a}\right) \hat{\mathbf{e}}_y + \operatorname{sech}\left(\frac{x}{a}\right) \hat{\mathbf{e}}_z \right], \quad (63)$$

while the initial electric field is null everywhere. The physical parameters that set the proper conditions for the instability to grow are the current sheet thickness a , the magnetization $\Sigma = B_0^2/\rho_0$, the plasma beta $\beta = 2p_0/B_0^2$, the Alfvén velocity $v_a = B_0/\sqrt{B_0^2 + w_0} = B_0/\sqrt{B_0^2 + \rho_0 + 4p_0}$ obtained by assuming an ideal gas law with relativistic adiabatic index $\Gamma = 4/3$, and the Lundquist number $S = v_a L/\eta$, where η is the resistivity and L is the reference spatial scale of variation. In order to trigger the instability, $S \gg 1$.

Generalizing the MHD results obtained by [Pucci & Velli \(2014\)](#)

and [Landi et al. \(2015\)](#) to this regime, provided a sufficiently thin current sheet, the reconnection process is expected to occur on the ideal Alfvénic time scale $\tau_a = L/v_a$. The critical (inverse) aspect ratio determining this regime is

$$a = S^{-1/3} L. \quad (64)$$

In the limit of large S , the growth rate γ_{TM} of the instability becomes $\gamma_{\text{TM}} \approx 0.6v_a/L$, which, in a relativistic regime ($v_a \rightarrow c = 1$), results in a very efficient process commonly referred to as *ideal tearing instability*.

The initial equilibrium is perturbed by a small amplitude ($\epsilon = 10^{-4}$) variation in the magnetic field employing only one wavenumber k

$$\delta\mathbf{B} = \epsilon B_0 \operatorname{sech}\left(\frac{x}{a}\right) \begin{pmatrix} \cos(ky) \\ \frac{\sin(ky)}{ka} \tanh\left(\frac{x}{a}\right) \\ 0 \end{pmatrix}. \quad (65)$$

Following §5.5 of [Mignone et al. \(2019\)](#), we initialize the magnetic field in the xy plane with the vector potential

$$A_z = -B_0 \left[a \log\left(\cosh\frac{x}{a}\right) - \frac{\epsilon}{k} \sin(ky) \operatorname{sech}\left(\frac{x}{a}\right) \right]. \quad (66)$$

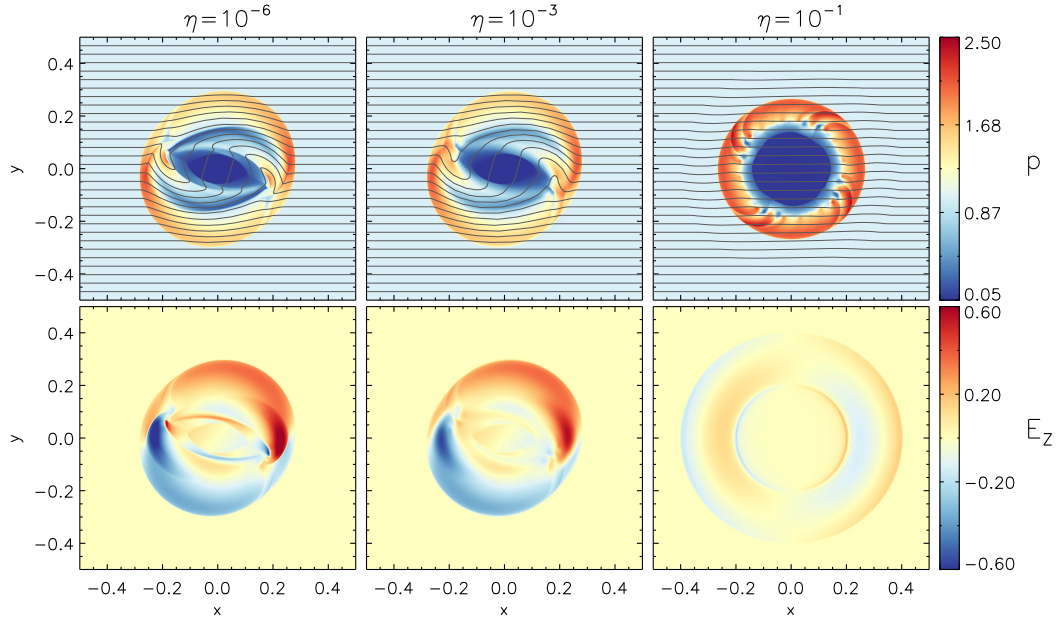


Figure 4. Snapshots of the gas pressure p (upper panels), and profiles of E_z (lower panels) for the resistive rotor test at its final time $t = 0.3$ at 400×400 grid points using the SSP3(4,3,3) IMEX time-stepping. From left to right, results correspond to computations with different resistivities $\eta = 10^{-6}$, $\eta = 10^{-3}$ and $\eta = 10^{-1}$.

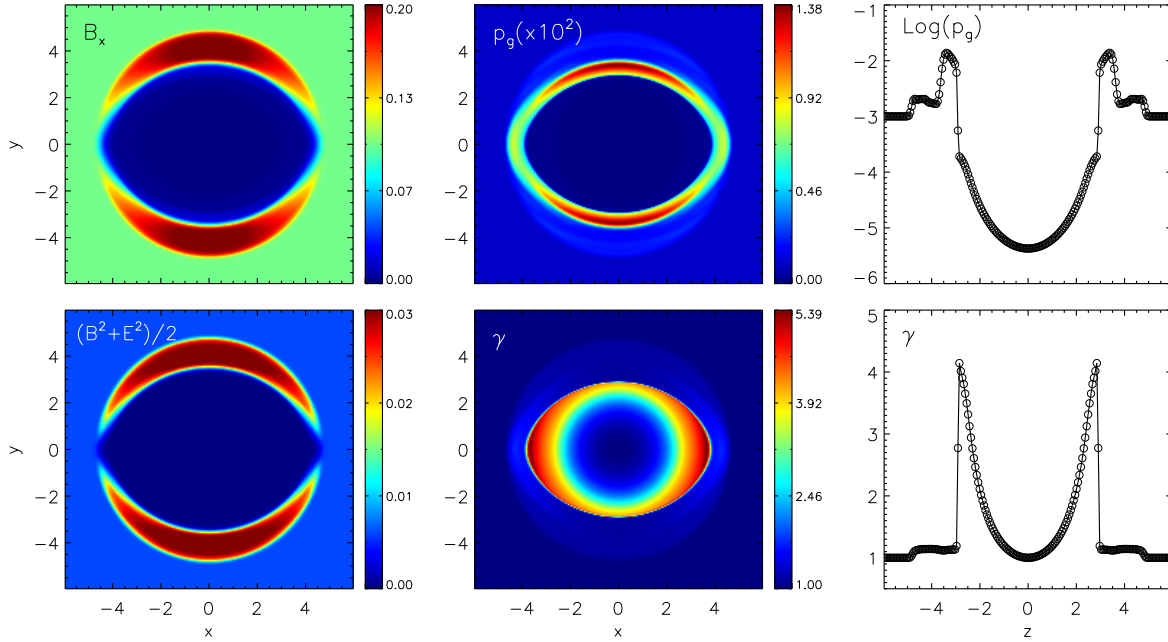


Figure 5. 3D Blast wave at $t = 4$ using $\eta = 10^{-6}$ and the CT scheme. In the top panels we show 2D slices in the xy plane of B_x (left), gas pressure p_g (middle) and its 1D profile along the z -axis (right). In the bottom panels we show 2D slices of the electromagnetic pressure (left), Lorentz factor (middle) together with its cuts of along the z -axis (right).

In accordance to the work developed by [Del Zanna et al. \(2016\)](#) and later resumed by [Mignone et al. \(2019\)](#), the linear theory predicts that the wavenumber associated with the fastest growing mode of the ideal tearing instability is $k_{\max} = 1.45^{1/6} = 14$. The corresponding growth rate is $\gamma_{\text{TM}} \approx 0.3$. Nonetheless, due to the neglect of the compressible terms in the linear approximation as presented

in [Del Zanna et al. \(2016\)](#), the maximum value of the dispersion relation is shifted to $k = 12$ with the consequent modification of the expected growth rate to $\gamma_{\text{TM}} \approx 0.27$. We therefore align with the works of [Del Zanna et al. \(2016\)](#), [Miranda-Aranguren et al. \(2018\)](#), and [Mignone et al. \(2019\)](#) and choose $k = 12$ for our simulations. Likewise, we set $L = B_0 = \Sigma = \beta = 1$, deriving therefore $\rho_0 = 1$,

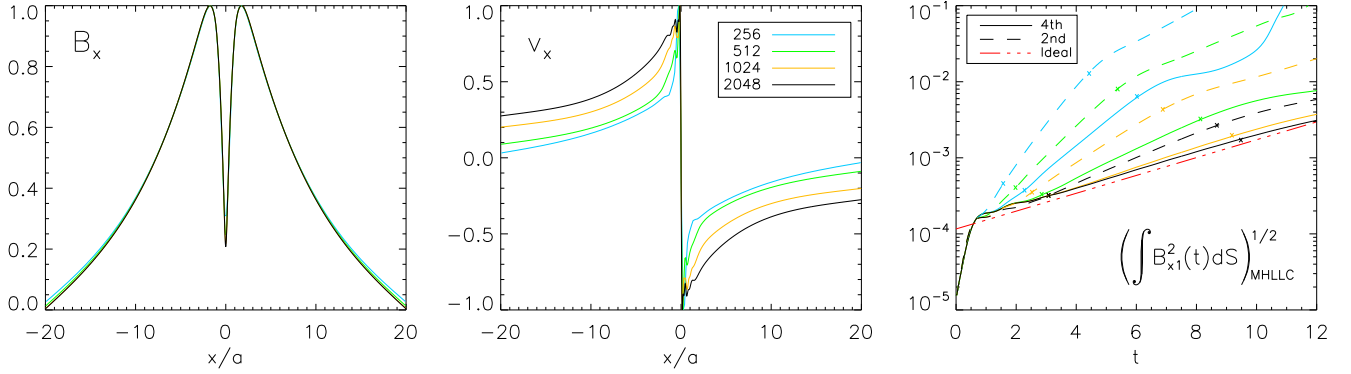


Figure 6. Horizontal cuts of the x -component of the magnetic field (left panel), and of the velocity (middle panel) for the tearing mode instability at $t = 10$. The profiles are normalized to unity and show the trends along $y = 0$ for the magnetic field (left panel), and along $\frac{3}{4}L_y$ for the velocity (middle panel). Each resolution ($N_x = \{256, 512, 1024, 2048\}$) is demarked with a different color. Measured growth rates (right panel) are plotted as solid (dashed) lines for 4th- (2nd-) order data and are compared to the ideal trend (dashed dotted line). Colorful crosses mark the time intervals for which each growth rate has been calculated.

$p_0 = 0.5$, $v_a = 0.5$, and $S = 10^6$. In this way $a = 0.01$, and $\eta = 5 \times 10^{-7}$. In order to recover the predicted growth rate, we perform a set of simulations with increasing resolution $N_x \times N_x/4$, ($N_x = \{256, 512, 1024, 2048\}$) on a rectangular computational domain with $x \in [-20a, 20a] = [-0.2, 0.2]$ and outflow boundary conditions, and $y \in [0, 0.523598]$ imposing periodicity along y . Simulations have been carried out until $t = 20$ using the IMEX SSP(4,3,3) time-stepping.

In the left and middle panels of Fig. 6 we plot the horizontal cuts at $y = 0$ of the x -components of the magnetic field (left panel), velocity (middle panel) at $t = 10$ for all resolutions. The magnetic field at all resolutions closely resembles the eigenfunction solutions presented by Del Zanna et al. (2016) (see Fig. 1 of that paper). The same holds for the velocity profile, although a more pronounced dependency on resolution is observed along with some clipping. Following Miranda-Aranguren et al. (2018), and Mignone et al. (2019) we measure the growth rate by first computing

$$\gamma(t) = \frac{1}{2} \log \left(\int B_x^2(t) dS \right), \quad (67)$$

which we plot, as a function of time, in the right panel of Fig. 6 (solid lines) along with 2nd-order data from Mignone et al. (2019) (dotted lines) for each resolution. The growth rate is then computed from a linear fit of Eq. (67) while the red dashed-dotted line represents the ideal value ($\gamma_{\text{TM}} \simeq 0.27$). Table 1 compares the results obtained with the 2nd- and 4th-order scheme (middle and right columns, respectively). For each slope, a different time-window has been chosen in order to properly fit the linear growth of the fastest growing mode (crosses in Fig. 6) during the first linear phase. While both the 2nd- and 4th-order schemes show systematic convergence towards the predicted value, the latter requires approximately half of the resolution (or less) to reproduce the results of the former. The best agreement is reached with the 4th-order scheme using 2048 zones.

4.6 3D Kelvin-Helmholtz Instability

As a final application benchmark, we consider a 3D version of Kelvin-Helmholtz instability in relativistic MHD (see, e.g. Bucciantini & Del Zanna 2006) as presented in paper I and earlier, in 2D, also by Mizuno (2013); Beckwith & Stone (2011). At $t = 0$, we prescribe a double shear layer configuration with non-uniform density and

Resolution	2 nd -order	4 th -order
256 × 64	1.19	0.75
512 × 128	0.89	0.44
1024 × 256	0.58	0.30
2048 × 512	0.38	0.27

Table 1. Growth rates of the linear phase of the tearing instability as measured from 2nd-order and 4th-order simulation data, listed by resolution. The measured growth rates refer to the onset of the first linear phase of the instability. The time intervals chosen to evaluate each slope are marked as crosses in the right panel of Fig. 6.

constant magnetic field:

$$\begin{aligned} \rho &= \frac{1 + \tanh \phi(y)}{2} \rho_h + \frac{1 - \tanh \phi(y)}{2} \rho_l, \\ \mathbf{v} &= v_{\text{sh}} \tanh \phi(y) \hat{\mathbf{e}}_x + A_0 [\text{sign}(y) \sin(2\pi x) \hat{\mathbf{e}}_y + \zeta \hat{\mathbf{e}}_z] f(y), \\ \mathbf{B} &= (\sqrt{2p\sigma\mu_p}, 0, \sqrt{2p\sigma\mu_t}), \end{aligned} \quad (68)$$

where $v_{\text{sh}} = 1/2$ is the shear velocity, $a = 0.01$ is the shear thickness, $\phi(y) = (|y| - 1/2)/a$ while $A_0 = 0.1$ is the perturbation amplitude and ζ is a random number in the range $[-1, 1]$. The function

$$f(y) = e^{-\phi^2 a^2 / \alpha^2} \quad (69)$$

(with $\alpha = 0.1$) is used to damp the perturbations as we move away from the two interface located at $y = \pm 1/2$. The parameters μ_p and μ_t control the in plane ($\mu_p = 0.01$) and out of plane ($\mu_t = 1$) magnetic field strength. We set resistivity to $\eta = 1/\sigma = 10^{-5}$ and evolve the system until $t = 30$ using the MHLLC Riemann solver. Following paper I, we perform simulations on the Cartesian domain $x, z \in [-1/2, 1/2]$ and $y \in [-1, 1]$ with uniform grid resolution $N \times 2N \times N$, with $N = 128$ (low-resolution) and $N = 256$ (high resolution).

Simulations have been repeated with both the high-order scheme - employing IMEX SSP3(4,3,3) time-stepping - as well as using also the 2nd-order scheme presented in paper I, based on piecewise

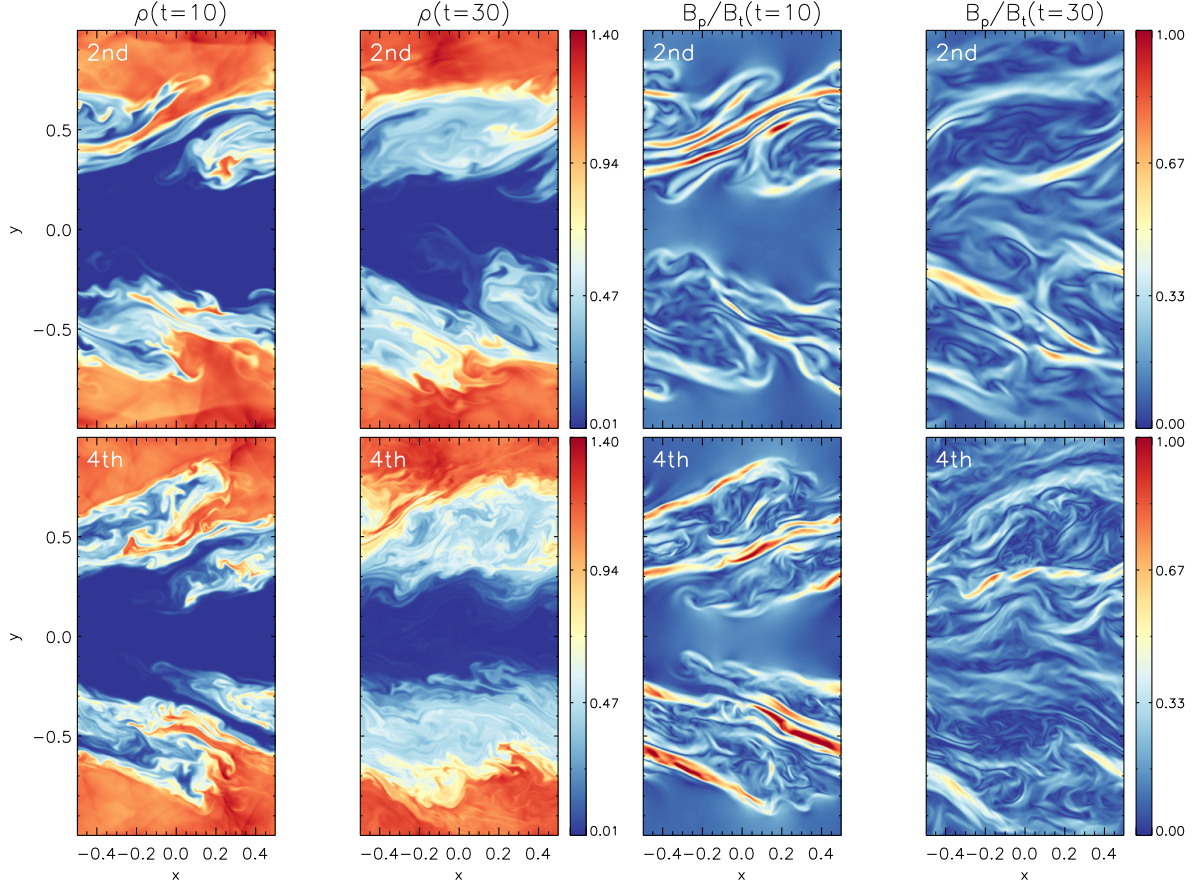


Figure 7. 2D slice-cut of the density and poloidal to toroidal magnetic field at $z = 0$ for the 3D Kelvin-Helmholtz instability at $t = 10$ and 30 at the resolution of $256 \times 512 \times 256$ zones. Here $B_p = \sqrt{B_x^2 + B_y^2}$.

linear reconstruction and second-order IMEX time-stepping. For the 4th-order method we employ order reduction (linear).

The time evolution of the instability can be observed in Fig. 7 where we show 2D slices at $z = 0$ for density (1st and 2nd row from top) and poloidal to toroidal magnetic field (3rd and 4th) with $N = 256$. The large-scale motion remains confined along the initial shear direction and the turbulent state is characterized by sheet-like thin structures, where most of the magnetic field energy is trapped. These rounded slabs remain roughly parallel to the xz plane although significant medium scale structures develop in this direction for $t \gtrsim 20$ around the shear layer.

A direct measure of the growth rate, quantified by $\Delta v_y = (\max(v_y) - \min(v_y))/2$, is shown in the top-left panel of Fig. 8 for both the 2nd and 4th-order simulations at low and high resolutions (blue and red colors, respectively). As noticed in paper I (see Fig. 11 of that paper), with the MHLLC Riemann solver, an increase in resolution (or scheme accuracy) is accompanied by a gradual reduction of the growth rate, until convergence is finally reached. This is also the case here and clearly visible with the 2nd-order method (red lines) but only marginally with the 4th-order scheme which shows better convergence properties at low resolution. A quantitative measure of the growth rate, in the range given by the circle symbols in the figure, yields indeed ≈ 2.94 and ≈ 2.14 for the 2nd-order scheme (low and high resolution, respectively) and ≈ 2.17 and ≈ 2.31 for the 4th-order scheme.

The enhanced dissipation of electromagnetic and kinetic energies

(top middle and right panels in Fig. 8) using our high-order scheme stems from the increased turbulence that comes from having an effective dissipation at scales smaller than the low-order case. In this sense, the performance of our high-order scheme at low resolutions ($N_x = 128$) already outperforms the one obtained by the 2nd-order scheme at twice the resolution.

The amount of small-scale features is an indirect measurement of the numerical dissipation, which we quantify through the spectral energy density,

$$P(k_x) = \int |\mathcal{F}(k_x, y, z)|^2 dy dz, \quad (70)$$

where $\mathcal{F}(k_x, y, z)$ is the 1D fast Fourier transform of the density taken across the x dimension. $P(k_y)$ and $P(k_z)$ are constructed similarly, by corresponding index permutations. Results, shown in the bottom rows of Fig. 8 ($P(k_y)$ and $P(k_z)$), indicate that large-scale modes are better resolved with the 4th-order scheme.

5 SUMMARY

We have presented a genuinely 4th-order finite volume algorithm for the solution of the resistive relativistic MHD equations in multiple dimensions. To our knowledge, this is one of the few contributions addressing the design of 4th-order methods based on an IMEX approach for multidimensional PDEs with stiff terms.

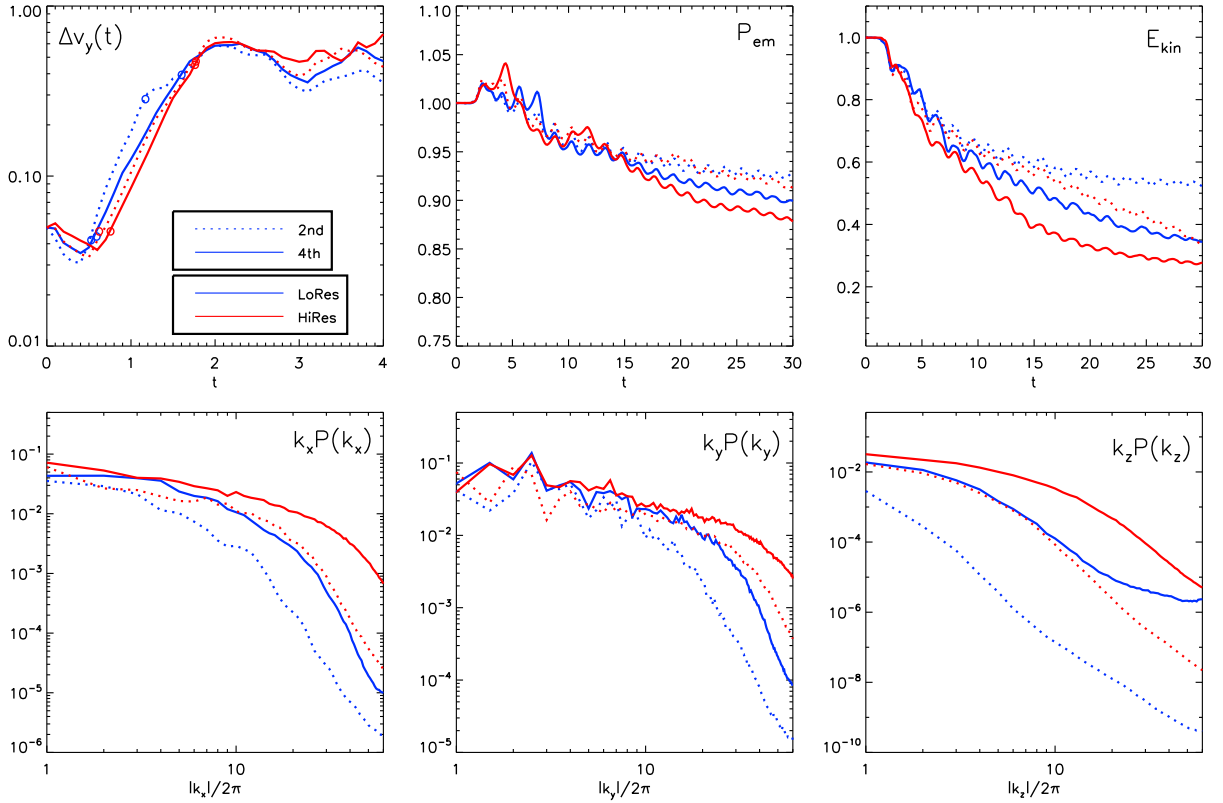


Figure 8. Top panels: growth rate (left) and volume-integrated electromagnetic $P_{\text{em}} = (\mathbf{B}^2 + \mathbf{E}^2)/2$ (middle) and kinetic $E_{\text{kin}} = \rho\gamma(\gamma - 1)$ (right) as a function of time for the 3D Kelvin-Helmholtz instability. Circles in the top-left plot mark the time windows used to compute the growth rate. Bottom panels: from left to right, spectral energy densities in the x , y and z -direction at $t = 15$. Solid and dashed lines are used for the 4th and 2nd order schemes while blue and red are used for the resolution of $128 \times 256 \times 128$ and $256 \times 512 \times 256$ zones, respectively.

High-order quadrature rules to obtain volume, surface or line averages are evaluated using appropriate Simpson rules, as outlined in the seminal paper by [McCorquodale & Colella \(2011\)](#). Point values are recovered from volume (or surface) averages following the opposite procedure. Fourth-order spatial accuracy is achieved by reconstructing point values (rather than 1D volume averages) using the modified WENO-Z reconstruction of [Berta et al. \(2024\)](#), while for temporal integration, we have implemented and compared the 3rd-order Runge Kutta IMEX SSP3(4,3,3) scheme of [Pareschi & Russo \(2003, 2005\)](#) with the 4th-order IMEX-ARK4(3)7L[2]SA_1 scheme of [Kennedy & Carpenter \(2019\)](#) (ARK). The divergence-free condition is ensured by evolving magnetic fields according to the constrained transport formalism, while electric field is treated as a volume average quantity. Equations are evolved in conservation form, requiring the solution of a Riemann problem between discontinuous left and right states at zone interfaces. Our scheme employs only 3 ghost zones, and thus a more compact stencil when compared to its previous version ([Berta et al. 2024](#)).

Numerical benchmarks in two and three dimensions demonstrate the accuracy of the method along with reduced numerical dissipation. For smooth problems our results show superior accuracy and faster convergence when compared to standard 2nd-order schemes. While the ARK4 retains the temporal 4th-order accuracy for smooth problems, we found in our experience that the 3rd-order SSP scheme is more robust for lower values of the resistivity, $\eta \lesssim 10^{-5}$ and thus preferable for highly stiff problems.

The scheme can also cope with complex flow features including

steep gradients and discontinuous waves, although the spatial order of the scheme may have to be locally reduced (“fallback” approach) so as to enhance robustness in critical regions. To identify such regions, we employ the discontinuity detector proposed in [Berta et al. \(2024\)](#), based on the ratio of derivative, specifically designed to detect high-frequency oscillations typically arising in proximity of a discontinuous front.

The employment of genuinely 4th-order methods may represent a major upgrade in the field of astrophysical plasma computations, allowing more accurate computations at a reduced cost.

ACKNOWLEDGEMENTS

Computational resources were provided by the Centro di Competenza sul Calcolo Scientifico (C3S) of the University of Torino (c3s.unito.it).

This project has received funding from the European Union’s Horizon Europe research and innovation programme under the Marie Skłodowska-Curie grant agreement No. 101064953 (GR-PLUTO).

This work has received funding from the European High Performance Computing Joint Undertaking (JU) and Belgium, Czech Republic, France, Germany, Greece, Italy, Norway, and Spain under grant agreement No 101093441 (SPACE).

This paper is supported by the Fondazione ICSC, Spoke 3 Astrophysics and Cosmos Observations. National Recovery and Resilience

Plan (Piano Nazionale di Ripresa e Resilienza, PNRR) Project ID CN_00000013 “Italian Research Center on High-Performance Computing, Big Data and Quantum Computing” funded by MUR Missione 4 Componente 2 Investimento 1.4: Potenziamento strutture di ricerca e creazione di “campioni nazionali di R&S (M4C2-19)” - Next Generation EU (NGEU).

The partial support from Gruppo Nazionale Calcolo Scientifico-Istituto Nazionale di Alta Matematica (GNCS-INdAM) and MIUR-PRIN Project 2022, No. 2022KKJP4X “Advanced numerical methods for time dependent parametric partial differential equations with applications” is also acknowledged.

DATA AVAILABILITY

The data underlying this article will be shared on reasonable request to the corresponding author.

REFERENCES

- Ascher U. M., Ruuth S. J., Spiteri R. J., 1997, *Applied Numerical Mathematics*, 25, 151
- Balsara D. S., Spicer D. S., 1999, *Journal of Computational Physics*, 149, 270
- Beckwith K., Stone J. M., 2011, *ApJS*, 193, 6
- Berta V., Mignone A., Bugli M., Mattia G., 2024, *Journal of Computational Physics*, 499, 112701
- Borges R., Carmona M., Costa B., Don W. S., 2008, *Journal of Computational Physics*, 227, 3191
- Boscarino S., Russo G., Semplice M., 2018, *Computers & Fluids*, 169, 155
- Boscheri W., Pareschi L., 2021, *Journal of Computational Physics*, 434, 110206
- Brecht S. H., Lyon J., Fedder J. A., Hain K., 1981, *Geophys. Res. Lett.*, 8, 397
- Bucciantini N., Del Zanna L., 2006, *A&A*, 454, 393
- Bucciantini N., Del Zanna L., 2013, *MNRAS*, 428, 71
- Bugli M., Del Zanna L., Bucciantini N., 2014, *MNRAS*, 440, L41
- Carpenter M., Kennedy C., Bijl H., et al. 2005, *J. Sci. Comput.*, 25, 157
- Cheong P. C.-K., Pong D. Y. T., Yip A. K. L., Li T. G. F., 2022, *ApJS*, 261, 22
- Conde S., Gottlieb S., Grant Z., et al. 2017, *J. Sci. Comput.*, 73, 677
- Dedner A., Kemm F., Kröner D., Munz C.-D., Schnitzer T., Wesenberg M., 2002, *Journal of Computational Physics*, 175, 645
- Del Zanna L., Bucciantini N., Londrillo P., 2003, *A&A*, 400, 397
- Del Zanna L., Zanotti O., Bucciantini N., Londrillo P., 2007, *A&A*, 473, 11
- Del Zanna L., Bugli M., Bucciantini N., 2014, in Pogorelov N. V., Audit E., Zank G. P., eds, *Astronomical Society of the Pacific Conference Series Vol. 488, 8th International Conference of Numerical Modeling of Space Plasma Flows (ASTRONUM 2013)*. p. 217 ([arXiv:1401.3223](https://arxiv.org/abs/1401.3223)), doi:10.48550/arXiv.1401.3223
- Del Zanna L., Papini E., Landi S., Bugli M., Bucciantini N., 2016, *MNRAS*, 460, 3753
- Dionysopoulou K., Alic D., Palenzuela C., Rezzolla L., Giacomazzo B., 2013, *Phys. Rev. D*, 88, 044020
- Dumbser M., Zanotti O., 2009, *Journal of Computational Physics*, 228, 6991
- Evans C. R., Hawley J. F., 1988, *ApJ*, 332, 659
- Felker K. G., Stone J. M., 2018, *Journal of Computational Physics*, 375, 1365
- Kennedy C. A., Carpenter M. H., 2019, *Applied Numerical Mathematics*, 136, 183
- Komissarov S. S., 2007, *MNRAS*, 382, 995
- Landi S., Del Zanna L., Papini E., Pucci F., Velli M., 2015, *ApJ*, 806, 131
- Londrillo P., del Zanna L., 2004, *Journal of Computational Physics*, 195, 17
- Mattia G., Del Zanna L., Bugli M., Pavan A., Ciolfi R., Bodo G., Mignone A., 2023, *A&A*, 679, A49
- McCorquodale P., Colella P., 2011, *Commun. Appl. Math. Comput. Sci.*, 6, 1
- Mignone A., Bodo G., 2005, *MNRAS*, 364, 126
- Mignone A., Bodo G., 2006, *MNRAS*, 368, 1040
- Mignone A., Del Zanna L., 2021, *Journal of Computational Physics*, 424, 109748
- Mignone A., Plewa T., Bodo G., 2005, *ApJS*, 160, 199
- Mignone A., Bodo G., Massaglia S., Matsakos T., Tesileanu O., Zanni C., Ferrari A., 2007, *ApJS*, 170, 228
- Mignone A., Zanni C., Tzeferacos P., van Straalen B., Colella P., Bodo G., 2012, *ApJS*, 198, 7
- Mignone A., Mattia G., Bodo G., 2018, *Physics of Plasmas*, 25, 092114
- Mignone A., Mattia G., Bodo G., Del Zanna L., 2019, *MNRAS*, 486, 4252
- Miranda-Aranguren S., Aloy M. A., Rembiasz T., 2018, *MNRAS*, 476, 3837
- Mizuno Y., 2013, *ApJS*, 205, 7
- Munz C. D., Omnes P., Schneider R., Sonnendrücker E., Voß U., 2000, *Journal of Computational Physics*, 161, 484
- Nakamura K., Miyoshi T., Nonaka C., Takahashi H. R., 2023, *European Physical Journal C*, 83, 229
- Palenzuela C., Lehner L., Reula O., Rezzolla L., 2009, *MNRAS*, 394, 1727
- Pareschi L., Russo G., 2003, in Hou T., Tadmor E., eds, *Hyperbolic Problems: Theory, Numerics, Applications: Proceedings of the Ninth International Conference on Hyperbolic Problems*. Springer Berlin Heidelberg, pp 241–251, doi:10.1007/978-3-642-55711-8_21
- Pareschi L., Russo G., 2005, *Journal of Scientific Computing*, 25, 129
- Pucci F., Velli M., 2014, *ApJ*, 780, L19
- Tomei N., Del Zanna L., Bugli M., Bucciantini N., 2020, *MNRAS*, 491, 2346
- Verma P. S., Teissier J.-M., Henze O., Müller W.-C., 2019, *MNRAS*, 482, 416
- Yee K., 1966, *IEEE Transactions on Antennas and Propagation*, 14, 302

APPENDIX A: EXPLICIT BUTCHER TABLEAUX

The following tables list the tableaux for the explicit (left), and implicit (right) coefficients for the IMEX-SSP3(4,3,3) L-stable scheme (see also Pareschi & Russo (2003, 2005), Table 6), and for the IMEX-ARK4(3)7L[2]SA₁ of Kennedy & Carpenter (2019). More specifically, the explicit form of Butcher's tableaux for the IMEX-SSP3(4,3,3) consists in:

$$\begin{array}{c|cccc}
 0 & 0 & 0 & 0 & 0 \\
 0 & 0 & 0 & 0 & 0 \\
 1 & 0 & 1 & 0 & 0 \\
 1/2 & 0 & 1/4 & 1/4 & 0 \\
 \hline
 & 0 & 1/6 & 1/6 & 2/3
 \end{array}
 \quad
 \begin{array}{c|cccc}
 \alpha & \alpha & 0 & 0 & 0 \\
 0 & -\alpha & \alpha & 0 & 0 \\
 1 & 0 & 1-\alpha & \alpha & 0 \\
 1/2 & \beta & \eta & 1/2-\beta-\eta-\alpha & \alpha \\
 \hline
 & 0 & 1/6 & 1/6 & 2/3
 \end{array}
 \tag{A1}$$

where $\alpha = 0.24169426078821$, $\beta = 0.06042356519705$, and $\eta = 0.12915286960590$. Similarly, the full form of the Butcher's tableaux for the IMEX-ARK4(3)7L[2]SA₁ consists in:

$$\begin{array}{c|cccccccc}
 0 & 0 & 0 & 0 & 0 & 0 & 0 & 0 \\
 \tilde{c}_2 & \tilde{a}_{21} & 0 & 0 & 0 & 0 & 0 & 0 \\
 \tilde{c}_3 & \tilde{a}_{31} & \tilde{a}_{32} & 0 & 0 & 0 & 0 & 0 \\
 \tilde{c}_4 & \tilde{a}_{41} & \tilde{a}_{42} & \tilde{a}_{43} & 0 & 0 & 0 & 0 \\
 \tilde{c}_5 & \tilde{a}_{51} & \tilde{a}_{52} & \tilde{a}_{53} & \tilde{a}_{54} & 0 & 0 & 0 \\
 \tilde{c}_6 & \tilde{a}_{61} & \tilde{a}_{62} & \tilde{a}_{63} & \tilde{a}_{64} & \tilde{a}_{65} & 0 & 0 \\
 \tilde{c}_7 & \tilde{a}_{71} & \tilde{a}_{72} & \tilde{a}_{73} & \tilde{a}_{74} & \tilde{a}_{75} & \tilde{a}_{76} & 0 \\
 \hline
 & 0 & 0 & \tilde{w}_3 & \tilde{w}_4 & \tilde{w}_5 & \tilde{w}_6 & \kappa
 \end{array}
 \quad
 \begin{array}{c|cccccccc}
 0 & 0 & 0 & 0 & 0 & 0 & 0 & 0 \\
 c_2 & \kappa & \kappa & 0 & 0 & 0 & 0 & 0 \\
 c_3 & a_{31} & a_{32} & \kappa & 0 & 0 & 0 & 0 \\
 c_4 & a_{41} & a_{42} & a_{43} & \kappa & 0 & 0 & 0 \\
 c_5 & a_{51} & a_{52} & a_{53} & a_{54} & \kappa & 0 & 0 \\
 c_6 & a_{61} & a_{62} & a_{63} & a_{64} & a_{65} & \kappa & 0 \\
 c_7 & a_{71} & a_{72} & a_{73} & a_{74} & a_{75} & a_{76} & \kappa \\
 \hline
 & 0 & 0 & w_3 & w_4 & w_5 & w_6 & \kappa
 \end{array}
 \tag{A2}$$

where $\kappa = 0.1235$. The remaining 21 explicit (\tilde{a}) and the 20 implicit coefficients (a) are, respectively:

$$\begin{array}{l}
 \tilde{a}_{21} = \frac{247}{1000} = 0.247 \\
 \hline
 \tilde{a}_{31} = \frac{247}{4000} = 0.06175 \qquad \tilde{a}_{32} = \frac{2694949928731}{7487940209513} = 0.35990537495 \\
 \hline
 \tilde{a}_{41} = \frac{464650059369}{8764239774964} = 0.05301658458 \qquad \tilde{a}_{42} = \frac{878889893998}{2444806327765} = 0.35949264529 \\
 \tilde{a}_{43} = -\frac{952945855348}{12294611323341} = -0.07750922988 \\
 \hline
 \tilde{a}_{51} = \frac{476636172619}{8159180917465} = 0.05841715944 \qquad \tilde{a}_{52} = -\frac{1271469283451}{7793814740893} = -0.16313824817 \\
 \tilde{a}_{53} = -\frac{859560642026}{4356155882851} = -0.19732090979 \qquad \tilde{a}_{54} = \frac{1723805262919}{4571918432560} = 0.37704199852 \\
 \hline
 \tilde{a}_{61} = \frac{6338158500785}{11769362343261} = 0.5385303227 \qquad \tilde{a}_{62} = -\frac{4970555480458}{10924838743837} = -0.45497746895 \\
 \tilde{a}_{63} = \frac{3326578051521}{2647936831840} = 1.25629056234 \qquad \tilde{a}_{64} = -\frac{880713585975}{1841400956686} = -0.47828452721 \\
 \tilde{a}_{65} = -\frac{1428733748635}{8843423958496} = -0.16155888888 \\
 \hline
 \tilde{a}_{71} = \frac{760814592956}{3276306540349} = 0.23221715782 \qquad \tilde{a}_{72} = \frac{760814592956}{3276306540349} = 0.23221715782 \\
 \tilde{a}_{73} = -\frac{47223648122716}{6934462133451} = -6.80999437504 \qquad \tilde{a}_{74} = \frac{71187472546993}{9669769126921} = 7.36185855242 \\
 \tilde{a}_{75} = -\frac{13330509492149}{9695768672337} = -1.37487907794 \qquad \tilde{a}_{76} = \frac{11565764226357}{8513123442827} = 1.35858058491
 \end{array}
 \tag{A3}$$

and

$$\begin{aligned}
 a_{31} &= \frac{624185399699}{4186980696204} = 0.14907768747 & a_{32} &= \frac{624185399699}{4186980696204} = 0.14907768747 \\
 a_{41} &= \frac{1258591069120}{10082082980243} = 0.12483442871 & a_{42} &= \frac{1258591069120}{10082082980243} = 0.12483442871 \\
 a_{43} &= -\frac{322722984531}{8455138723562} = -0.03816885743 \\
 a_{51} &= -\frac{436103496990}{5971407786587} = -0.0730319403 & a_{52} &= -\frac{436103496990}{5971407786587} = -0.0730319403 \\
 a_{53} &= -\frac{2689175662187}{11046760208243} = -0.24343568716 & a_{54} &= \frac{4431412449334}{12995360898505} = 0.34099956776 \\
 a_{61} &= -\frac{2207373168298}{14430576638973} = -0.15296500088 & a_{62} &= -\frac{2207373168298}{14430576638973} = -0.15296500088 \\
 a_{63} &= \frac{242511121179}{3358618340039} = 0.07220562047 & a_{64} &= \frac{3145666661981}{7780404714551} = 0.40430630248 \\
 a_{65} &= \frac{5882073923981}{14490790706663} = 0.4059180788 \\
 a_{71} &= 0 & a_{72} &= 0 \\
 a_{73} &= \frac{9164257142617}{17756377923965} = 0.51611072831 & a_{74} &= -\frac{10812980402763}{74029279521829} = -0.14606356393 \\
 a_{75} &= \frac{1335994250573}{5691609445217} = 0.23473048589 & a_{76} &= \frac{2273837961795}{8368240463276} = 0.27172234973
 \end{aligned} \tag{A4}$$

where, for the sake of simplicity, the horizontal lines are used to highlight the different stages of the algorithm. From Eq. 23, the explicit form of the coefficients $\tilde{c} = c$ becomes:

$$\begin{aligned}
 \tilde{c}_2 &= \frac{247}{1000} = 0.247 & \tilde{c}_3 &= \frac{4276536705230}{10142255878289} = 0.42165537495 \\
 \tilde{c}_4 &= \frac{67}{200} = 0.335 & \tilde{c}_5 &= \frac{7}{40} = 0.075 \\
 \tilde{c}_6 &= \frac{7}{10} = 0.7 & \tilde{c}_7 &= 1
 \end{aligned} \tag{A5}$$

The Butcher's tableaux are finally completed by the coefficients $w = \tilde{w}$:

$$\begin{aligned}
 \tilde{w}_3 &= \frac{9164257142617}{17756377923965} = 0.51611072831 & \tilde{w}_4 &= -\frac{10812980402763}{74029279521829} = -0.14606356393 \\
 \tilde{w}_5 &= \frac{1335994250573}{5691609445217} = 0.23473048589 & \tilde{w}_6 &= \frac{2273837961795}{8368240463276} = 0.27172234973.
 \end{aligned} \tag{A6}$$

This paper has been typeset from a \LaTeX file prepared by the author.